Viscoplastic rimming flow inside a rotating cylinder

Thomasina V. Ball[1] and Neil J. Balmforth[2]

[1]*Mathematics Institute, University of Warwick, Coventry, CV4 7AL, UK*
[2]*Department of Mathematics, University of British Columbia*

(Dated: February 15, 2024)

Abstract

A theoretical analysis is presented for the flow of a Herschel-Bulkley fluid around the inside surface of a rotating cylinder, at rotation speeds for which the fluid largely collects in a prominent pool in the lower part of the cylinder. The analysis, based on lubrication theory, predicts the steady states typically reached after a small number of rotations. The analysis is also modified to consider the drainage of the film around a stationary cylinder, which allows an exploration of the dynamics when a rotating drum is suddenly stopped. The predictions of the theory are compared with experiments in which a Carbopol suspension is rotated inside an acrylic drum.

I. INTRODUCTION

The flow of a viscous fluid around the surface of a rotating cylinder has proved a popular configuration in which to study the fluid mechanics of coating flows[1–6]. Beginning with Moffatt[1], an initial point of interest was the development of a corner and shocks in leading-order lubrication theory, as a more uniform coating on the inside of a horizontal cylinder became increasingly influenced by gravity[2,3]. Such irregularities in the shape of the free surface become smoothed by surface tension, higher-order gravity effects, or over lengthscales violating the scale separation implicit in lubrication theory[4–7]. Instabilities leading to three-dimensional flow structures have also been of interest as illustrations of pattern formation[8–11].

A key drawback of the leading-order lubrication model used to study flows with weak gravitational effects is that it fails to deal with situations in which gravity plays a dominant role, dragging most of the coating fluid around the rotating cylinder into a pool sitting near the lowest point. This situation led Tirumkudulu & Acrivos[7] and Ashmore, Hosoi & Stone[4] to restructure the lubrication model, adding some important higher-order terms (incorporating either surface tension, gravity corrections, or both). The restructured model accounts for pooling at the bottom of the cylinder, together with the thin film that becomes drawn out of the pool, then coats the remainder of the cylinder surface before re-entering the pool. The draw-out and re-entry of the film at the edges of the pool correspond to the classical Landau-Levich problem and its variants[4,5,12,13].

Despite the prevalence of analyses employing Newtonian fluid, the coating flows that feature in a large number of industrial processes[14] often involve complex fluids. Partly with this in mind, a number of studies have explored rimming flows of viscoelastic fluids and suspensions (see Ref. 11). With more relevance to the present work, Johnson[3] considered coating by power-law fluids and Ross, Duffy & Wilson[15] generalized Moffatt's analysis to allow the coating fluid to have a yield stress. Neither of these studies, however, deal with situations with gravitational pooling at the bottom of the cylinder. When pooling does arise, that reservoir of fluid is not motionless, but continues to overturn driven by the rotation. In fact, for viscoplastic fluid, the resulting states have much in common with the steady surges encountered in laboratory experiments using inclined conveyor belts, designed to simulate geophysical flows[16–19]. The rotating drum arguably provides a simpler configuration to explore such surges, providing a key motivation for the present paper.

We organize the paper as follows: in section II we mathematically formulate the problem and use a shallow-layer approximation (lubrication theory) to derive a reduced model for the flow of a thin film of a viscoplastic fluid described by a model constitutive law (the Herschel-Bulkley law[20]) along a circular surface (*cf.* Refs. 21 and 22). That said, our formulation is more general, applying to any nearly horizontal, slowly varying surface and may therefore prove useful in other settings. However, by avoiding any geometrical approximations in the gravitational terms, the model also recovers the viscoplastic generalization of the leading-order lubrication analysis for a more uniform coating[1,15] in a different limit of the model's dimensionless parameters. Thus, by bridging between the two asymptotic limits, the model captures the dynamics of both the pool at the bottom of the cylinder and the residual film coating it elsewhere (*cf.* Ref. 7). In section III, we use the model to explore the steady rimming solutions that are predicted to develop within a rotating drum. We follow this up in section IV, with a discussion of the dynamics when the cylinder does not rotate, which allows us to explore what happens when a rotating cylinder is suddenly stopped. In particular, we consider how the coating drains to rest, which inevitably becomes controlled

by the yield stress (if one is present). The theoretical results are then compared with some laboratory experiments in section V. We conclude in section VI. The Appendix contains some details of the theoretical construction of steady rimming flows without surface tension (which is otherwise included in our model formulation).

II. THE MODEL

A. Formulation

Consider the flow of a two-dimensional, incompressible film of Bingham fluid on the inside of a cylinder of radius R, rotating anticlockwise with rate Ω. We neglect inertia, and represent the geometry of the cylinder using polar coordinates system $(\hat{r}, \theta)$, with $\theta = 0$ corresponding to the vertically down direction, as illustrated in figure 1(a). The shallow fluid layer coating the inner surface is described using a local curvilinear coordinate system $(\hat{s}, \hat{z})$ in which $\hat{s} = R\theta$ is arc length along the cylinder and $\hat{z} = R - \hat{r}$ (see figure 1(b)). The fluid velocity and pressure are $(\hat{u}(\hat{s}, \hat{z}), \hat{w}(\hat{s}, \hat{z}))$ and $\hat{p}(\hat{s}, \hat{z})$, satisfying

$$\frac{\partial \hat{u}}{\partial \hat{s}} + (1 - \kappa\hat{z})\frac{\partial \hat{w}}{\partial \hat{z}} - \kappa\hat{w} = 0, \tag{1}$$

$$\frac{\partial \hat{\tau}_{\rm ss}}{\partial \hat{s}} - \frac{\partial \hat{p}}{\partial \hat{s}} + (1 - \kappa\hat{z})\frac{\partial \hat{\tau}_{\rm sz}}{\partial \hat{z}} - 2\kappa\hat{\tau}_{\rm sz} = \rho g(1 - \kappa\hat{z})\sin\theta, \tag{2}$$

$$\frac{\partial \hat{\tau}_{\rm sz}}{\partial \hat{s}} + (1 - \kappa\hat{z})\left(\frac{\partial \hat{\tau}_{\rm zz}}{\partial \hat{z}} - \frac{\partial \hat{p}}{\partial \hat{z}}\right) + \kappa(\hat{\tau}_{\rm ss} - \hat{\tau}_{\rm zz}) = \rho g(1 - \kappa\hat{z})\cos\theta, \tag{3}$$

where the curvature is

$$\kappa = \frac{\partial \theta}{\partial \hat{s}} \equiv R^{-1}, \tag{4}$$

$\hat{\tau}_{\rm ij}$ is the deviatoric stress tensor, and subscripts (in Roman font) indicate tensor components. The Bingham law relates the stress to the strain rates by

$$\hat{\tau}_{\rm ij} = \left(\mu + \frac{\tau_{\rm Y}}{\hat{\dot{\gamma}}}\right)\hat{\dot{\gamma}}_{\rm ij} \qquad \text{for} \qquad \hat{\tau} > \tau_{\rm Y}, \tag{5}$$

and $\hat{\dot{\gamma}}_{\rm ij} = 0$ otherwise, where μ is the (plastic) viscosity, $\tau_{\rm Y}$ is the yield stress, and

$$\{\hat{\dot{\gamma}}_{\rm ij}\} = \begin{pmatrix} 2(\hat{u}_{\hat{s}} - \kappa\hat{w})/(1 - \kappa\hat{z}) & (\hat{w}_{\hat{s}} + \kappa\hat{u})/(1 - \kappa\hat{z}) + \hat{u}_{\hat{z}} \\ (\hat{w}_{\hat{s}} + \kappa\hat{u})/(1 - \kappa\hat{z}) + \hat{u}_{\hat{z}} & 2\hat{w}_{\hat{z}} \end{pmatrix}. \tag{6}$$

Here subscripts of $\hat{s}$ and $\hat{z}$ on the velocity components denote partial derivatives, and $\hat{\dot{\gamma}} = \sqrt{\frac{1}{2}\sum_{ij}\hat{\dot{\gamma}}_{\rm ij}\hat{\dot{\gamma}}_{\rm ij}}$ and $\hat{\tau} = \sqrt{\frac{1}{2}\sum_{ij}\hat{\tau}_{\rm ij}\hat{\tau}_{\rm ij}}$ denote the tensor second invariants.

We have further employed a hat notation to denote dimensional variables; this decoration is removed using suitable scalings in our non-dimensionalization of the problem below.

At the free surface of the fluid film, $\hat{z} = \hat{h}(\hat{s}, \hat{t})$, ignoring surface tension,

$$(1 - \kappa\hat{h})\hat{\tau}_{\rm sz} - (\hat{\tau}_{\rm ss} - \hat{p})\frac{\partial \hat{h}}{\partial \hat{s}} = (1 - \kappa\hat{h})(\hat{\tau}_{\rm zz} - \hat{p}) - \hat{\tau}_{\rm sz}\frac{\partial \hat{h}}{\partial \hat{s}} = 0 \tag{7}$$

and

$$\hat{w} = \frac{\partial \hat{h}}{\partial \hat{t}} + \frac{\hat{u}}{1 - \kappa\hat{h}}\frac{\partial \hat{h}}{\partial \hat{s}}. \tag{8}$$

On the cylinder, no slip demands that

$$\hat{u} = R\Omega \qquad \& \qquad \hat{w} = 0. \tag{9}$$

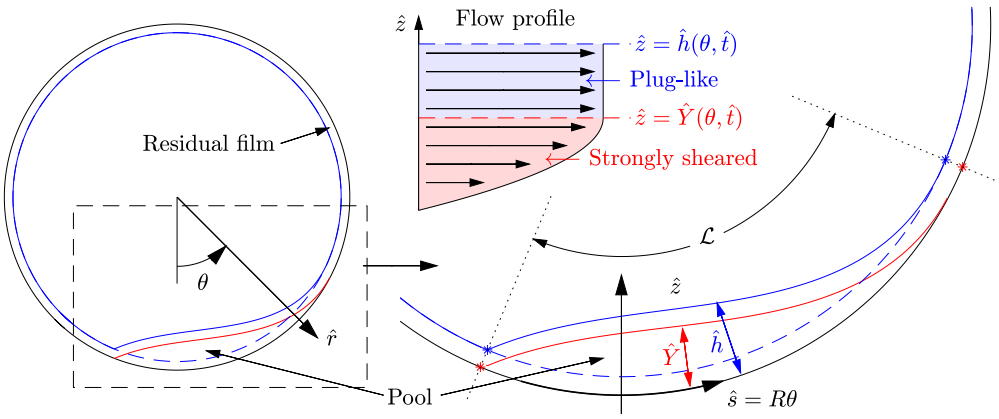

FIG. 1. A sketch showing the geometry of the rimming flow. The red and blue stars mark the ends of the "pool" over which most of the fluid collects and the depth $\hat{h}$ varies significantly; beyond these points there is a residual, potentially plugged up film. The pool has a typical length $\mathcal{L} \ll R$. Lubrication theory predicts that the flow profile takes a distinctive form in which a strongly sheared layer intervenes between the drum and a plug-like region, the "pseudo-plug", bordering the free surface; the strongly sheared layer has thickness $\hat{Y}$. Beyond the pool, one anticipates a residual, plugged-up film to coat the remainder of the cylinder (with $\hat{Y} = 0$).

B. Scaling

The pool at the bottom of the cylinder has a characteristic length $\mathcal{L}$ and a typical depth $\mathcal{H}$. The fluid is shallow, so that $\epsilon = \mathcal{H}/\mathcal{L} \ll 1$, and the pool occupies a small fraction of the circumference, $\mathcal{L} \ll R$; see figure 1. More specifically, to account properly for the effect of gravity on the pool, the gravitational force along the surface of the cylinder, $\rho g \sin\theta \sim \rho g \hat{s}/R$, must be comparable to hydrostatic pressure gradients in the fluid, $\hat{p}_\theta \sim \rho g \frac{\partial \hat{h}}{\partial \hat{s}}$.

Balancing the magnitudes of these two terms indicates that $\mathcal{H} = O(\epsilon^2 R)$ or $\mathcal{L} = O(\epsilon R)$. Furthermore, when the pool contains a significant fraction of the fluid, the pool's area, of $O(\mathcal{H}\mathcal{L})$, must be comparable to the total fluid area, $\pi R^2 f$, where $f \ll 1$ is the "fill fraction" of the drum. In other words, $\epsilon = O(f^{\frac{1}{3}})$.

We now remove the dimensions from the equations by defining the new variables,

$$s = \frac{\hat{s}}{\mathcal{L}}, \quad (z, h) = \frac{(\hat{z}, \hat{h})}{\mathcal{H}}, \quad u = \frac{\hat{u}}{R\Omega}, \quad w = \frac{\hat{w}}{\epsilon R\Omega}, \quad t_* = \frac{R\Omega\hat{t}}{\mathcal{L}}, \tag{10}$$

$$p = \frac{\hat{p}}{\rho g \mathcal{H}}, \quad \tau_{\mathrm{ij}} = \frac{\hat{\tau}_{\mathrm{ij}}}{\epsilon \rho g \mathcal{H}}, \quad \dot{\gamma}_{\mathrm{ij}} = \frac{\hat{\dot{\gamma}}_{\mathrm{ij}} \mathcal{H}}{R\Omega}. \tag{11}$$

To leading order, the dimensionless equations become

$$u_s + w_z = 0, \tag{12}$$

$$\frac{\partial \tau_{\mathrm{sz}}}{\partial z} - \frac{\partial p}{\partial s} = g_{\mathrm{s}} \equiv \frac{\sin\theta}{\epsilon}, \tag{13}$$

$$-\frac{\partial p}{\partial z} = g_{\mathrm{z}} \equiv \cos\theta. \tag{14}$$

Because the pool has a limited angular extent, $\epsilon^{-1}\sin\theta \sim s = O(1)$, and the gravity components $(g_{\rm s}, g_{\rm z})$ are both order one. Rather than introducing their leading order replacements, $(s, 1)$, however, we retain the trigometric functions in $(g_{\rm s}, g_{\rm z})$ in order to make contact with existing literature and allow the model to capture the dynamics of the residual film coating the cylinder outside the pool (see §II E).

The dimensionless, yielded version of the constitutive law is

$$\tau_{\rm ij} = \left(\Lambda_*^{-1} + \frac{{\rm Bi}_*}{\dot\gamma}\right)\dot\gamma_{\rm ij}, \quad \{\dot\gamma_{\rm ij}\} = \begin{pmatrix} 2\epsilon u_s + O(\epsilon^3) & u_z + O(\epsilon^2) \\ u_z + O(\epsilon^2) & 2\epsilon w_z \end{pmatrix}, \tag{15}$$

where the dimensionless parameters,

$$\Lambda_* = \frac{\rho g \mathcal{H}^3}{\mu \mathcal{L} R \Omega} \quad \text{and} \quad {\rm Bi}_* = \frac{\tau_{\rm Y}\mathcal{L}}{\rho g \mathcal{H}^2}. \tag{16}$$

Provided $u_z = O(1)$, equation (15) indicates that the shear stress dominates the other deviatoric stress components and the yield condition reduces to $|\tau_{\rm sz}| > {\rm Bi}_*$. In this situation, the fluid is relatively strongly sheared. There is, however, a second way to deal with the constitutive relation: if we take $u_z = O(\epsilon)$, we must retain all the components of the deformation rate tensor at the same $O(\epsilon)$ order. This leads to the perfectly plastic relation $\tau_{\rm ij} = {\rm Bi}_*\dot\gamma_{\rm ij}/\dot\gamma$ to leading order. Because this applies where $u_z = O(\epsilon)$, $|\tau_{\rm sz}| < {\rm Bi}_*$ and $\sqrt{{\tau_{\rm ss}}^2 + {\tau_{\rm sz}}^2} \sim {\rm Bi}_*$, the flow here is plug-like, but still yielded; this is Walton & Bittleston's pseudo-plug[23,24]. It turns out that shallow viscoplastic flows typically contain both a strongly sheared region and a pseudo-plug[22,24].

Finally, the surface boundary conditions reduce to

$$p = \tau_{\rm sz} = 0 \quad \text{and} \quad w = \frac{\partial h}{\partial t_*} + u\frac{\partial h}{\partial s}, \quad \text{on} \quad z = h. \tag{17}$$

The dimensionless no-slip conditions are

$$u = 1 \quad \text{and} \quad w = 0 \quad \text{on} \quad z = 0. \tag{18}$$

C. Reduction

Equations (13) and (14) imply that

$$p = g_{\rm z}(h - z) \quad \text{and} \quad \tau_{\rm sz} = -(g_{\rm s} + g_{\rm z}h_s)(h - z) \tag{19}$$

(bearing in mind that $p_s = g_{\rm z}h_s + O(\epsilon^2)$). Unless the entire film becomes plugged up, the flow therefore splits up into a sheared region near the cylinder, where

$$|\tau_{\rm sz}| > {\rm Bi}_*, \quad u_z = -\Lambda_*(g_{\rm s} + g_{\rm z}h_s)(Y - z), \quad Y = h - \frac{{\rm Bi}_*}{|g_{\rm s} + g_{\rm z}h_s|}, \quad 0 < z < Y, \tag{20}$$

and an overlying pseudo-plug with

$$|\tau_{\rm sz}| < {\rm Bi}_*, \quad u_z = O(\epsilon), \quad Y < z < h \tag{21}$$

(*cf.* figure 1). This furnishes the velocity profile,

$$u = \begin{cases} 1 - \frac{1}{2}\Lambda_*(g_{\rm s} + g_{\rm z}h_s)(2Y - z)z, & 0 < z < Y, \\ u_{\rm p} = 1 - \frac{1}{2}\Lambda_*(g_{\rm s} + g_{\rm z}h_s)Y^2, & Y < z < h, \end{cases} \tag{22}$$

and the angular flux

$$q_*(s, t_*) = \int_0^h u \, {\rm d}z = h - \tfrac{1}{6}\Lambda_*(g_{\rm s} + g_{\rm z}h_s)Y^2(3h - Y). \tag{23}$$

Mass conservation, integrated over the thickess of the film, then demands that

$$\frac{\partial h}{\partial t_*} + \frac{\partial q_*}{\partial s} = 0. \tag{24}$$

When Y, as defined in (20), approaches zero the pseudo-plug is predicted to fill the entire layer and the velocity vanishes. The condition, $h \leq {\rm Bi}_*/|g_{\rm s} + g_{\rm z}h_s|$, then corresponds to the creation of a genuine plug attached to the cylinder. In this situation, the flux q_* must equal h. In order to recover the correct flux from (23) we therefore replace the definition of Y in (20) by

$$Y = {\rm Max}\left(0, h - \frac{{\rm Bi}_*}{|g_{\rm s} + g_{\rm z}h_s|}\right). \tag{25}$$

Equations (23)-(25) adapt the shallow viscoplastic fluid model of Liu & Mei[21,22] to the rotating drum configuration. As written, however, the model in (23)-(24) is more general, applying to shallow viscoplastic flow over an arbitrarily shaped, nearly horizontal surface, as long as one revises the connection between arc length and angle (from $\hat{s} = R\theta$ to $\theta_{\hat{s}} = \kappa(\hat{s})$).

D. Inclusion of surface tension and shear thinning

When surface tension is included, we must modify the normal force condition at $z = h$. In particular, the surface pressure, $p = P$ at $z = h$, no longer vanishes and we replace (19) with

$$p = P + g_{\rm z}(h - z) \quad \text{and} \quad \tau_{\rm sz} = -(g_{\rm s} + g_{\rm z}h_s + P_s)(h - z), \tag{26}$$

where the surface pressure is

$$P = constant - \frac{\sigma h_{ss}}{\rho g \mathcal{L}^2}, \tag{27}$$

the surface tension is σ and we take the dimensionless group $\sigma/(\rho g \mathcal{L}^2)$ (related to a Bond number) to be order one. The reduction of the equations now follows as before, but for the addition of P_s to the hydrostatic pressure gradient $g_{\rm s} + g_{\rm z}h_s$.

If we use the Herschel-Bulkley law instead of Bingham, the key change is the replacement of the effective viscosity $(\mu + \tau_{\rm Y}\hat{\dot{\gamma}}^{-1})$ in (5) with $(K\hat{\dot{\gamma}}^{n-1} + \tau_{\rm Y}\hat{\dot{\gamma}}^{-1})$. The consistency K and power-law index n can now be employed to redefine the viscosity scale as $\mu = K(R\Omega/\mathcal{H})^{n-1}$, and the non-dimensionalization of the model then proceeds as above. The dimensionless viscosity function is $[(\dot{\gamma}/\Lambda_*)^n + {\rm Bi}_*]\dot{\gamma}^{-1}$, with

$$\Lambda_* = \Omega^{-1}\left(\frac{\epsilon\rho g R}{K}\right)^{\frac{1}{n}}\left(\frac{\mathcal{H}}{R}\right)^{1+\frac{1}{n}}, \tag{28}$$

and the flux in (23) becomes

$$q_* = h - \frac{n\Lambda_* Y^{1+\frac{1}{n}}[(1+2n)h - nY]}{(n+1)(2n+1)}|g_{\rm s} + g_{\rm z}h_s + P_s|^{\frac{1}{n}}\ \mathrm{sgn}(g_{\rm s} + g_{\rm z}h_s + P_s). \tag{29}$$

More details of the reduction for the Herschel-Bulkley model can be found in[19,22] There is also a relatively thin buffer between the strongly sheared region and the pseudo-plug over which the solutions for the two become matched, but which needs no explicit consideration[23–25].

E. Summary

We now return to the original angular variable θ in place of s, which has the awkward feature that the length of the pool $\mathcal{L}$ is selected as the scale during non-dimensionalization, but this is not known ahead of time. We further follow Ashmore *et al.*[4] in defining some new variables based on the fill fraction of the cylinder, f, which for a shallow film is

$$f = \int_0^{2\pi} \hat{h}(\theta, \hat{t})\frac{\mathrm{d}\theta}{\pi R}. \tag{30}$$

In particular, we set

$$t = \Omega\hat{t} \equiv \frac{\mathcal{L}t_*}{R}, \quad \eta(\theta,t) = \frac{\hat{h}}{Rf} \equiv \frac{\mathcal{H}h}{Rf}, \quad \mathcal{Y}(\theta,t) = \frac{\mathcal{H}Y}{Rf}, \quad q(\theta,t) = \frac{\mathcal{H}q_*}{Rf}, \tag{31}$$

which indicate that

$$\eta_t + q_\theta = 0, \quad q = Q(\eta,\Gamma) = \eta - \frac{\Lambda\mathcal{Y}^{1+\frac{1}{n}}|\Gamma|^{\frac{1}{n}}}{n+1}[(1+2n)\eta - n\mathcal{Y}]\ \mathrm{sgn}(\Gamma), \tag{32}$$

along with the constraint,

$$1 = \int_0^{2\pi} \eta(\theta,t)\frac{\mathrm{d}\theta}{\pi}, \tag{33}$$

where

$$\Gamma = \sin\theta + f\eta_\theta\cos\theta - S\eta_{\theta\theta\theta}, \qquad \mathcal{Y} = \mathrm{Max}\left(0, \eta - \frac{\mathrm{Bi}}{|\Gamma|}\right), \tag{34}$$

$$\Lambda = \frac{n\Lambda_*\mathcal{L}^{\frac{1}{n}}(fR)^{1+\frac{1}{n}}}{(2n+1)\mathcal{H}^{1+\frac{2}{n}}} = \frac{nf^{1+\frac{1}{n}}}{(2n+1)\Omega}\left(\frac{\rho g R}{K}\right)^{\frac{1}{n}}, \qquad \mathrm{Bi} = \frac{\tau_{\rm Y}}{\rho g R f} \equiv \frac{\mathcal{H}^2\mathrm{Bi}_*}{R\mathcal{L}f}, \qquad S = \frac{\sigma f}{\rho g R^2} \tag{35}$$

and we have extended our subscript notation to partial time and angle derivatives.

A final modification that is possible is to make the non-asymptotic replacement,

$$S\eta_{\theta\theta\theta} \to \left[\frac{S(\eta+\eta_{\theta\theta})}{(1+f^2\eta_\theta^2)^{3/2}}\right]_\theta, \tag{36}$$

for the surface tension term in (34), a commonly employed device that seeks to better incorporate surface curvature[4,13]. We follow this suit in the computations reported below, although it has little impact on the solutions presented. Indeed, surface tension altogether has a relatively minor effect. That said, the evolution equation (32) is problematic when

$S = 0$ because the resulting nonlinear diffusion equation has a negative diffusivity (being proportional to $\cos\theta$) in the upper half of the cylinder. This awkward behaviour is conveniently removed when surface tension is included, as in the Newtonian version of the problem[4,5].

With the definition of the new variables and parameters, the scales $\mathcal{H}$ and $\mathcal{L}$ now disappear from the formulation of the model (indicating that it is no longer necessary to select either). Nevertheless, our asymptotic reduction applies in a certain limit of the problem corresponding to $\epsilon = \frac{\mathcal{H}}{\mathcal{L}} \ll 1$. In particular, in our shallow-layer limit, the dimensionless parameters and variables in (32)-(33) are not all order one, with their size depending on how ϵ ultimately becomes related to the fill fraction f (formally, $\epsilon = O(f^{\frac{1}{3}})$).

Note that the model in (32)-(33) also applies in a different limit of the coating problem, corresponding to $f \ll 1$ and $\theta = O(1)$. In this case, the film coats the cylinder more uniformly, and a different asymptotic reduction leads to (32)-(33), but with the sole modification that one must drop the free-surface gravity term, $f\eta_\theta \cos\theta$, in comparison to the other terms, $\sin\theta - S\eta_{\theta\theta\theta}$, in Γ. This alternative reduction corresponds to the Herschel-Bulkley generalization of the leading-order lubrication model considered by Moffat and others (as accomplished for a Bingham fluid by Ross *et al.*[15]).

Such considerations lead us to now relax any constraints on the parameters in (32)-(33), allowing us to consider both the pool and residual film, or coatings in which the lengthscale $\mathcal{L}$ is larger, and indeed comparable to R. In other words, we use our model to bridge between the limit considered by Moffatt and others, and the one underlying our asymptotic reduction (*cf.* Ref. 7).

III. MODEL SOLUTIONS

We solve the evolution equation (32) as an initial-value problem, choosing a fixed grid in angle and employing spectral differentiation matrices to evaluate spatial derivatives[26]. This reduces (32) to a set of coupled ordinary differential equations (ODEs), which we integrate using Matlab's stiff integrator ODE15s. To ease the computation and take into account any unyielded plugs, we regularize the constitutive law by replacing the second relation in (34) by

$$\mathcal{Y}_\varepsilon = \eta - \frac{\mathrm{Bi}}{|\Gamma|}, \qquad \mathcal{Y} = \tfrac{1}{2}\left(\mathcal{Y}_\varepsilon + \sqrt{\varepsilon^2 + \mathcal{Y}_\varepsilon^2}\right), \tag{37}$$

where ε is a regularization parameter. Practically we take ε to be 10^{-4} or smaller, and verify that its precise value has little effect on the solutions other than smoothing out some of the finer scale features near the yield points.

As found by Ashmore *et al.* in the Newtonian version of the problem, solutions rapidly converge to steady state whenever an appreciable pool forms near the bottom of the cylinder. These steady states can be found more directly by abandoning (32) and setting instead $q = Q(\eta, \Gamma) = \textit{constant}$. With surface tension, this corresponds to a differential eigenvalue problem with periodic boundary conditions and the constraint (33), which can be solved using Matlab's BVP4c solver (again regularizing via (37)). The flux condition must be inverted to write Γ in terms of η and q as part of this solution strategy. The BVP4c steady solution solver has the advantage of exploiting an adaptive grid to resolve any finer features in the solution.

A. Sample solutions

Figure 2 displays sample steady solutions for a Bingham fluid ($n = 1$) at fixed $\Lambda = 10$, $f = 0.01$ and $S = 10^{-4}$ with varying Bi. Plotted are the angular profiles of the free surface, $h(\theta)$, and fake yield surface, $\mathcal{Y}(\theta)$. At these parameter settings, surface tension has only a minor effect and a narrow pool forms near the bottom of the cylinder. The solutions feature prominent pseudo-plugs over the pool and film, which thicken to become true plugs (where $\mathcal{Y} = 0$) over sections to the left of the pool and at the top of the cylinder. Over these true plugs, $\eta = q$. The pseudo-plugs are shaded according to the local plug speed, and the yield points where $\mathcal{Y} \to 0$ are indicated. Insets show illustrations of how the pool would appear within the rotating drum. Increasing the yield stress from the Newtonian limit reduces the size of the pool and drags it up the side, whilst thickening the residual film coating the remainder of the cylinder; the pool disappears for $\mathrm{Bi} \to \frac{1}{2}$. This trend, which is shown in more detail in figure 3 for a wider set of solutions, is similar to an increase in rotation rate in the Newtonian problem[4].

A sequence more like an experimental series is shown in figure 4, which shows solutions with fixed rheological parameters ($\mathrm{Bi} = 0.158$ and $n = 0.38$), fill fraction ($f = 0.0838$) and surface tension ($S = 10^{-4}$), but varying rotation rate (Λ). The trends with increasing rotation rate (decreasing Λ) reproduce those for increasing yield stress in figure 2. The choices for f, n and Bi in figure 4 actually correspond to the experiments discussed below in §V. The choice for S, though, is too large by a factor of about four, assuming that the experimental fluid, Carbopol, has a surface tension slightly lower than that of water[27,28]. This is not significant, given the minor role played by surface tension in the solutions.

To emphasize this point, we show solutions with varying S in figure 5, for a Bingham fluid with $(\Lambda, f, \mathrm{Bi}) = (10, 0.01, 0.1)$. The solution with $S = 10^{-4}$ is still slightly sensitive to this surface tension parameter; once S is decreased to 10^{-5} or smaller, however, only some of the finer details of the solutions depend on S. This figure also includes a construction of the steady solution without surface tension altogether, as described more fully in the Appendix. The suite of solutions shown in figure 4, with the Herschel-Bulkley parameters chosen to match the experiments, are even less sensitive to S, as highlighted by the match of the peak depth and position between solutions computed for $S = 10^{-4}$ and $S = 0$ (unlike in figure 3, where there is a minor difference).

B. Anatomy of the steady, pooled solution

More details of a steady, pooled solution are displayed in figure 6. A similar picture, but for a solution in which the pool has been dragged well up the side of the cylinder, is shown in figure 7. The latter example corresponds to the viscoplastic generalization of one of the Newtonian solutions with shocks considered in previous literature (*e.g.* Refs. 4 and 5). Note that the significantly pooled example in figure 6 possesses a substantial recirculation cell (as revealed by the streamline pattern also drawn), whereas the more shock-like case in figure 7 displays no recirculation.

As illustrated in figure 6, the pool is mostly relatively narrow and of high amplitude for $f \ll 1$ and $\Lambda \gg 1$, remaining localized to the bottom of the cylinder ($\theta \ll 1$). The flux relation $q = Q(\eta, \Gamma)$ then indicates that Γ must be $O(\Lambda^{-n})$ over this region. A local approximation of the first relation in (34) then implies that $f\eta_\theta + \theta \approx 0$, provided surface tension remains unimportant. Hence, $\eta \approx \eta_{max} - \theta^2/(2f)$, which reflects how the surface

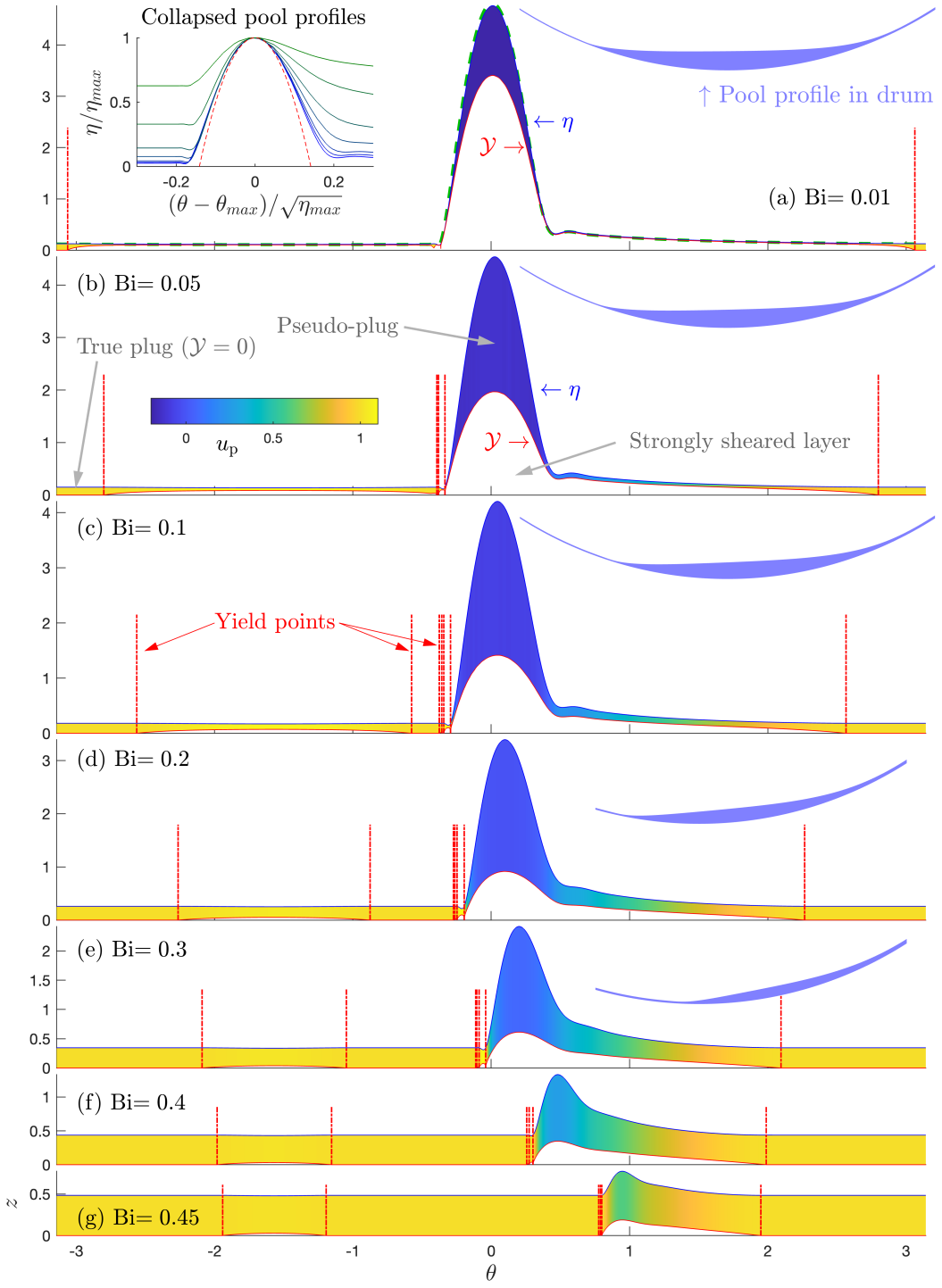

FIG. 2. Steady solutions with varying Bi (as indicated) for $(\Lambda, f, n, S) = (10, 0.01, 1, 10^{-4})$. Shown are the positions of the free surface η and yield surface $\mathcal{Y}$, with the pseudo-plug and plug shaded according to the local value of plug speed, $u_p \equiv 1 - \frac{3}{2}\Lambda\Gamma\mathcal{Y}^2$. The vertical dot-dashed lines show the yield points. In (a), the dashed line shows the corresponding Newtonian solution, and the left-hand inset replots all the surface profiles (from blue to green) using the scaled variables η/η_{max} and $(\theta-\theta_{max})/\sqrt{\eta_{max}}$, and comparing with the approximation in (38) (red dashed line). The right-hand insets show the profiles of some of the solutions as they would appear inside the drum.

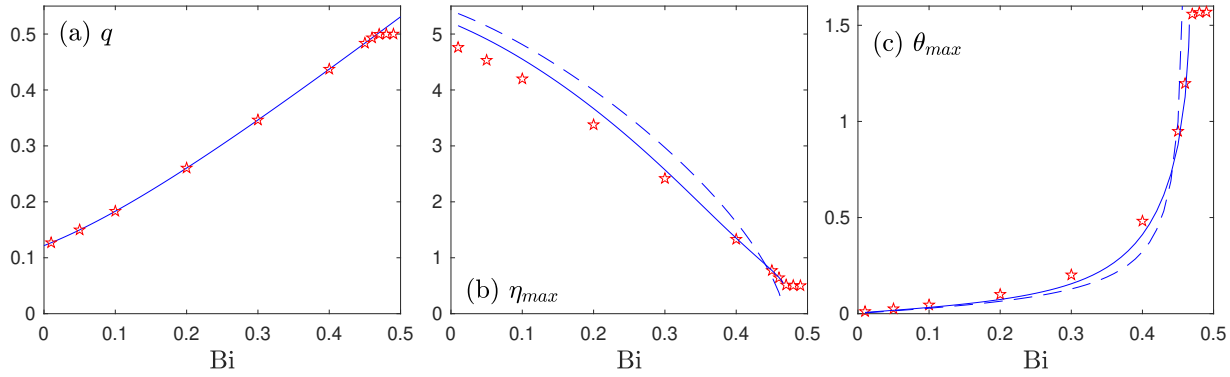

FIG. 3. (a) Flux, q, and (b,c) peak height and position, η_{max} and θ_{max}, plotted against Bi for $(\Lambda, f, S) = (10, 0.01, 10^{-4})$. The solid line in (a) shows the prediction from (40). The solid lines in (b) and (c) show the results from the analysis of the Appendix in which surface tension is neglected, and the dashed lines show the predictions from (44) and (46).

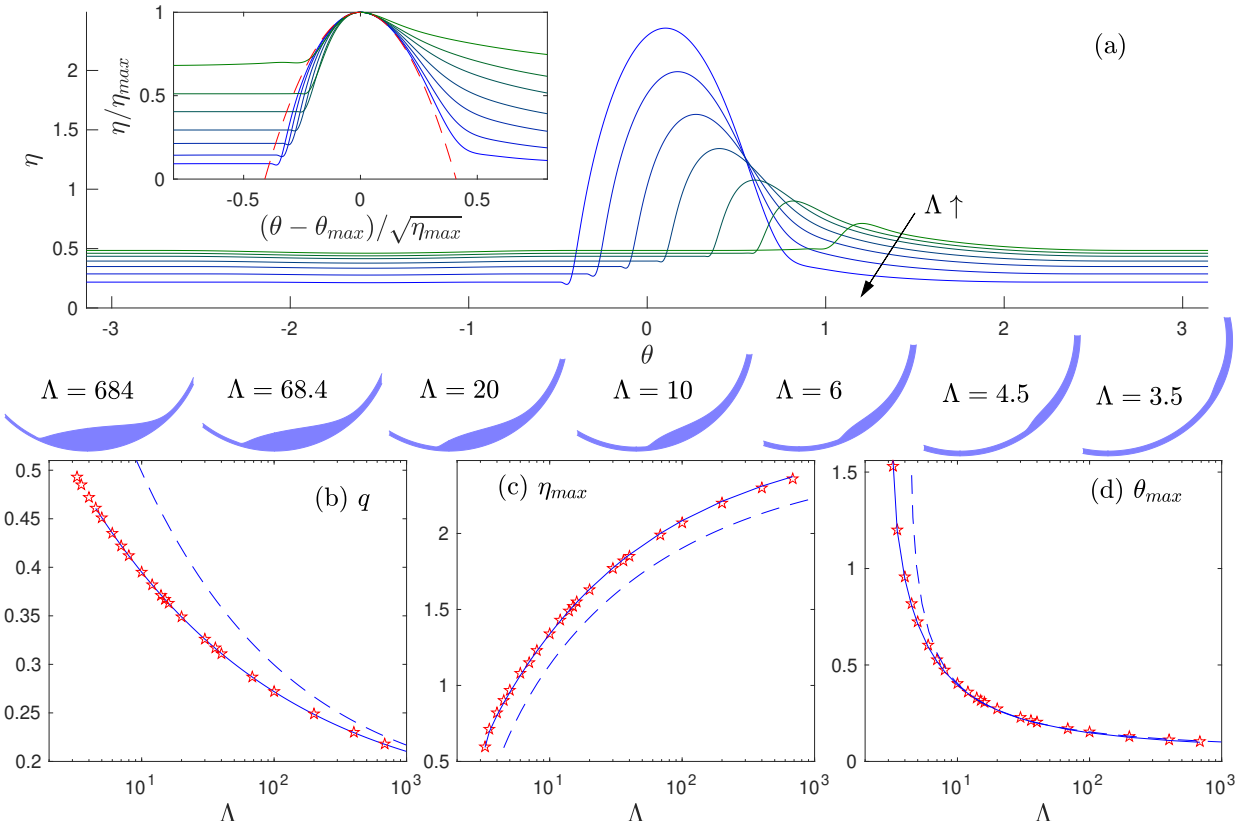

FIG. 4. Steady solutions with increasing Λ (from green to blue) for $(f, \mathrm{Bi}, n, S) = (0.0838, 0.158, 0.38, 10^{-4})$. In (a) the free surface profile is shown for the values of Λ indicated. The upper left inset shows a collapse of these profiles over the pool, along with the prediction in (38). In (b)-(d), the flux q, and the peak height and position, η_{max} and θ_{max}, are plotted against Λ for a wider set of solutions (stars). The solid lines in (b) shows the predictions from (41), and the solid lines in (c,d) indicate the results from the $S = 0$ analysis of the Appendix. The dashed lines in (b,c,d) show the predictions from (42), (44) and (46).

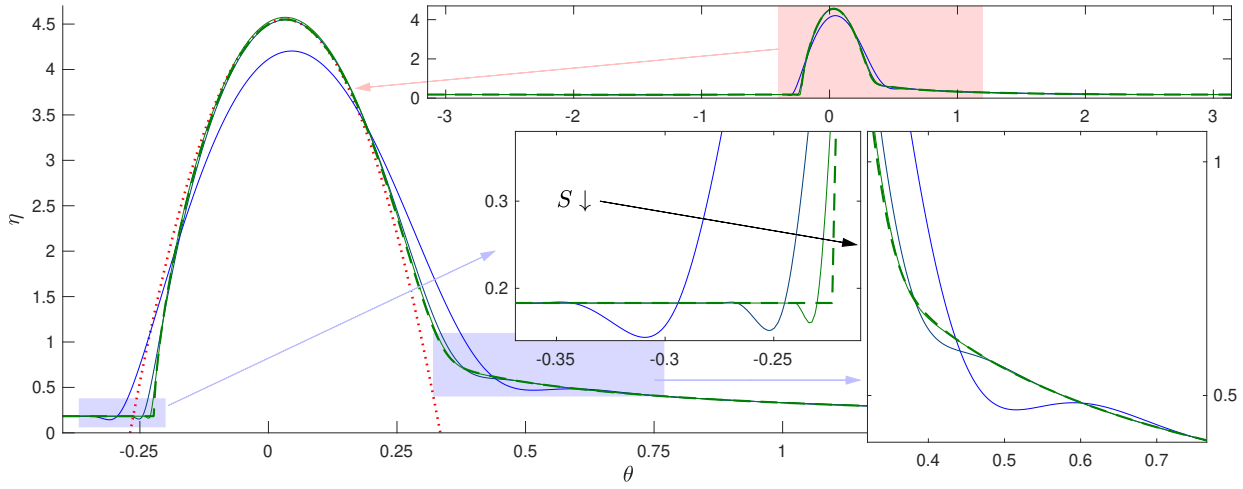

FIG. 5. Steady solutions with $S = 10^{-4}$, 10^{-5} and 10^{-6} (solid, from blue to green), for $(\Lambda, \mathrm{Bi}, n, f) = (10, 0.1, 1, 0.01)$. The dashed line shows the construction of the Appendix for $S = 0$. The dotted line shows the approximation (38). The main panel shows the pool solutions; the insets show the entire solutions and magnifications near the borders of the pool (as indicated by the shading and arrows).

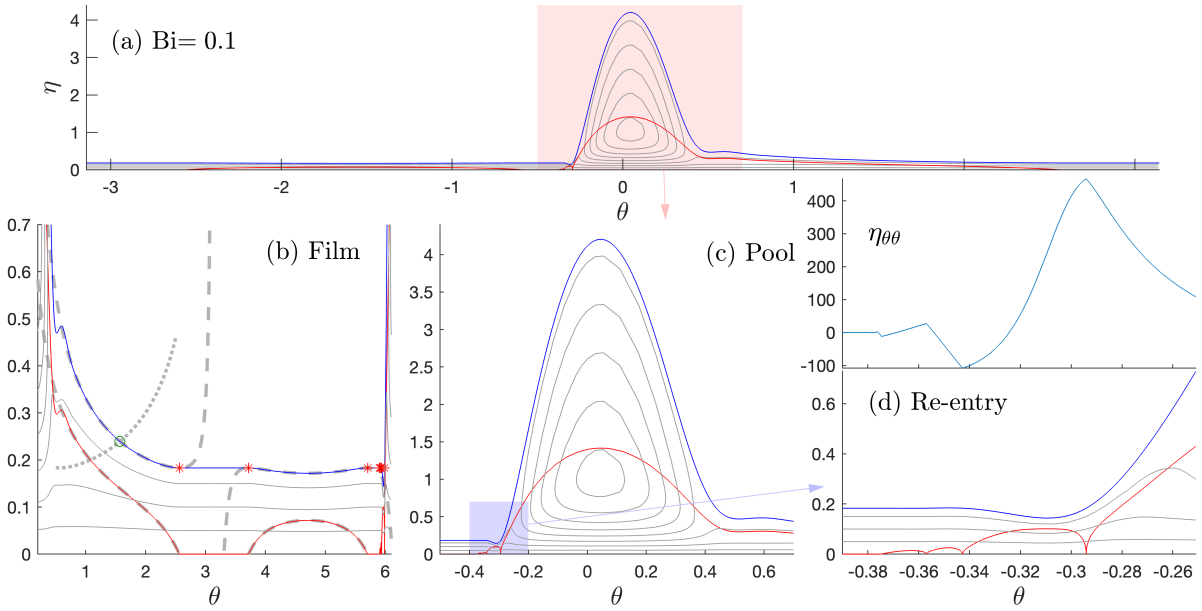

FIG. 6. Anatomy of the solution with $(\Lambda, f, \mathrm{Bi}, n, S) = (10, 0.01, 0.1, 1, 10^{-4})$. Plotted are η (blue) and $\mathcal{Y}$ (red), along with a selection of streamlines (light grey solid lines). In (b), the residual film is shown in more detail. The dashed grey lines show the root of the cubic $q = \textit{constant}$ with $\Gamma = \sin\theta$, to which the solution converges over the film; the grey dotted line shows a second root, which intersects the first at the green circle at $\theta = \frac{1}{2}\pi$. A magnification of the pool is shown in (c). Details of where the film re-enters the pool are plotted in (d), along with $\eta_{\theta\theta}$.

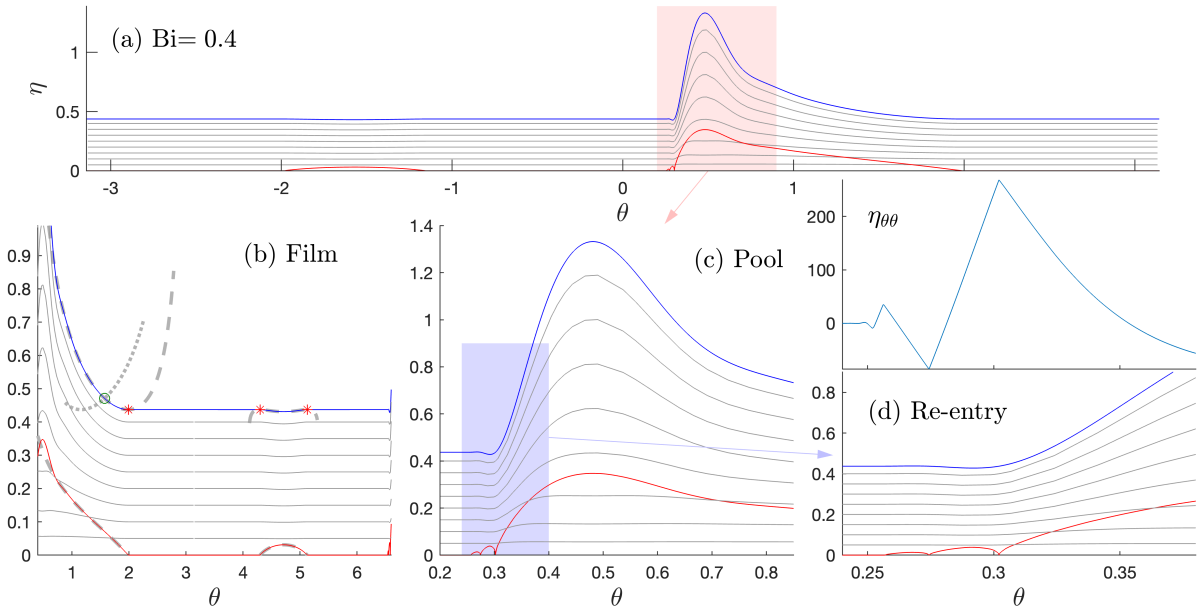

FIG. 7. A similar set of plots to figure 6, but for Bi = 0.4.

of the pool becomes relatively flat, and can be cast as a more formal asymptotic solution relevant to the limit $\Lambda \gg 1$. The pool solutions in figures 2, 4 and 5 match fairly well with the approximation, even when the pool becomes shifted away from $\theta_{max} = 0$, as long as we make the replacement $\theta^2 \to (\theta - \theta_{max})^2$. *i.e.* the solution for the pool is approximately

$$\eta \approx \eta_{max} - \frac{(\theta - \theta_{max})^2}{2f}. \tag{38}$$

The pool therefore has a width of approximately $2\sqrt{2f\eta_{max}}$, and contains about $\frac{4}{3}\eta_{max}\sqrt{2f\eta_{max}}$ of the total fluid area.

Outside the pool, over the residual film coating the remainder of the cylinder, we have $q = Q(\eta, \Gamma) = constant$ and $\Gamma \approx \sin\theta$, which for $n = 1$ boils down to a cubic equation for η:

$$\Lambda \sin\theta(\eta^3 - \tfrac{3}{2}b\eta^2 + \tfrac{1}{2}b^3) - \eta + q = 0, \quad b = \frac{\mathrm{Bi}}{|\sin\theta|}. \tag{39}$$

As shown in figures 6 and 7, the steady solutions to the full problem do indeed converge to one of the roots of the cubic over the film. Importantly, at $\theta = \frac{1}{2}\pi$ ($\Gamma \approx 1$), two of the roots intersect, in order to allow the film thickness to continue to decrease to the right of the pool (*cf.* Refs. 2 and 5). The intersection (*i.e.* the presence of a double root) implies that

$$q = \frac{1}{4}\Lambda^{-\frac{1}{2}}\left[\left(\beta^2 + \frac{4}{3}\right)^{\frac{3}{2}} + 2\beta - \beta^3\right], \quad \beta = \Lambda^{\frac{1}{2}}\mathrm{Bi}, \tag{40}$$

as illustrated in figure 3(a). For $\beta \ll 1$, we recover the Newtonian result $q \sim \frac{1}{4}\Lambda^{-\frac{1}{2}}(\frac{4}{3})^{\frac{3}{2}}$. When $\beta \gg 1$, we enter instead a plastic limit (*cf.* §III C) with $q \sim \mathrm{Bi}$. When $n < 1$, similar predictions follow from demanding

$$Q(\eta, \sin\theta) - q = 0 \qquad \text{and} \qquad \frac{\partial}{\partial\eta}Q(\eta, \sin\theta) = 0, \tag{41}$$

although the results are not explicit and must be found by solving an algebraic problem numerically. As long as $\mathrm{Bi}\Lambda^{\frac{n}{n+1}} \gg 1$, the second relation in (41) can be solved in the limit $\mathcal{Y} \ll 1$, to find $\mathcal{Y} \sim [(2+n^{-1})\Lambda\eta]^n \sim [(2+n^{-1})\Lambda\mathrm{Bi}]^n$, and the first relation then implies that

$$q \approx \mathrm{Bi} + \frac{1}{n+1}\left[\frac{n}{(2n+1)\mathrm{Bi}\Lambda}\right]^n. \tag{42}$$

These results indicate that $\eta = O(q)$ over the film, which is small when there is a significant pool near the bottom of the cylinder. Consequently, the fluid is mostly contained in the pool, and so

$$\frac{4}{3}\eta_{max}\sqrt{2f\eta_{max}} \sim \pi \qquad \text{or} \qquad \eta_{max} \sim \left(\frac{9\pi^2}{32f}\right)^{\frac{1}{3}}, \tag{43}$$

which is independent of all parameters but f. The pool solutions plotted in figures 2-7 have not yet reached the limit in (43), and still depend on Bi and Λ. To advance past the limitations of (43), we keep track of the contribution of the residual film to the fluid area. In particular, by taking $\eta \approx q$ over the film, and retaining its contribution to the constraint (33) (*i.e.* adding $2\pi q$ to the left of the first relation in (43)), we arrive at

$$\eta_{max} \sim \left[\frac{9\pi^2(1-2q)^2}{32f}\right]^{\frac{1}{3}}. \tag{44}$$

Note also that the peak position, where $\Gamma = \sin\theta_{max}$ if $|S\eta_{\theta\theta\theta}| \ll 1$, follows from solving

$$q = Q(\eta_{max}, \sin\theta_{max}), \tag{45}$$

or (39) if $n = 1$. Approximately (when $\mathcal{Y}$ is small and $\eta_{max} \gg q$), we have

$$\sin\theta_{max} \sim \frac{\mathrm{Bi}}{\eta_{max}} + \left[\frac{(n+1)\mathrm{Bi}}{(2n+1)\Lambda\eta_{max}^{2+\frac{1}{n}}}\right]^{\frac{n}{n+1}}. \tag{46}$$

The predictions from (40), (44) and (46) are included in figure 3, and those from (42), (44) and (46) in figure 4. The predictions for the flux in (40) or (41) follow from discarding the $O(f)$ and surface tension terms from (34), a relatively accurate approximation as seen in figure 3(c). By contrast, the cruder approximations leading to (42), (44) and (46) introduce noticeable discrepancies with the numerical solutions in figure 3(b,c) and 4(b,c,d).

Finally we comment on the structure of the transition layers between the pool and residual film. In figures 2 and 4-7, the layer to the right contains mild undulations owing to the importance of surface tension; by analogy with the Newtonian problem, the asymptotic structure of these standing capillary waves is likely complicated[5], although the impact of the yield stress is not known. Nevertheless, these undulations disappear once the surface tension parameter S becomes sufficiently small (*cf.* the Appendix), leaving a relatively smooth transition. The layer to the left of the pool is more complicated: here the solutions with surface tension ($S > 0$) again pass through a wavetrain. In the viscoplastic problem, this wavetrain takes a distinctive form, with the curvature $\eta_{\theta\theta}$ converging to decaying sawtooth wave (see figures 6 and 7), as explored further in a related problem by Jalaal *et al.*[29,30]. The convergence to the limit $S \to 0$ is also further obscured by the presence of discontinuities in surface slope for $S = 0$ (see figure 5 and the Appendix), which must be smoothed on a sufficiently small scale by surface tension whenever S is finite.

C. Plastic limit

The solutions presented above indicate that the most significant effect of the yield stress arises at the slowest rotation rates ($\Lambda \gg 1$): as evident from figure 4 and equation (46), the viscoplastic fluid coating converges to a shape with finite slope in this limit. This feature contrasts sharply with the Newtonian problem, for which the free surface must become horizontal when surface tension is not significant.

For fluid with a yield stress, $\Lambda \to \infty$ actually corresponds to the "perfectly plastic" limit, wherein the yield stress dominates the viscous stress except over a thin boundary layer adjacent to the cylinder. That is, $\mathcal{Y} \to 0$, with the pseudo-plug spanning most of the fluid depth and a good fraction of the residual film fully plugged up. Because $\mathcal{Y} \to 0$, the yielded regions of the limiting state satisfy $\eta \approx \mathrm{Bi}/|\Gamma|$, or the ODE,

$$\eta_\theta \approx \frac{\mathrm{Bi} - \eta \sin\theta}{f\eta\cos\theta}, \tag{47}$$

when surface tension is neglected. This ODE can be integrated from a yield point $\theta = \theta_{_L}$ at the left border of the pool to the right-hand yield point $\theta = \theta_{_R}$, which approaches $\theta = \frac{1}{2}\pi$ in the plastic limit. The slope is discontinuous at $\theta_{_L}$, but smoother at $\theta_{_R}$ (*cf.* figures 2, 6 and 7). The position of the left-hand yield point $\theta_{_L}$ must be selected to satisfy the constraint (33) (practically, this can be accomplished by adopting a trial value for $\theta_{_L}$, computing the solution and the implied fluid area, then performing Newton iteration until the constraint is satisfied). Sample solutions constructed in this fashion are illustrated in figure 8. With surface tension, the construction is more complicated in view of the behaviour near the left-hand yield point (*cf.* figure 6(d)).

For $f \ll 1$, the pool is approximately given by (38) (as follows from neglecting Bi on the right-hand side of (47) and taking $\theta \ll 1$), whereas the film is given by $\eta = \mathrm{Bi}/\sin\theta$ (dropping the left-hand side of (47)). The pool then has the maximum depth in (43), or more accurately (44) with $q = \mathrm{Bi}$, and an almost flat surface with a finite inclination given by $\sin\theta_{max} = \mathrm{Bi}/\eta_{max}$ (see figure 8(b,c)). These results can be seen much more readily by first observing that, given the fill fraction f, the maximum depth of the segment of the drum occupied by the pool is approximately (43), or (44) if the residual film is taken into account. Then, per unit width, the net gravitational force on the central cross-section of the segment (through $\theta = \theta_{max}$) has an angular component $\rho g \hat{h}_{max} \sin\theta_{max}$ that must be largely balanced by the yield stress, $\tau_{_Y}$. That is,

$$\sin\theta_{max} = \frac{\tau_{_Y}}{\rho g \hat{h}_{max}} \equiv \frac{\mathrm{Bi}}{\eta_{max}}. \tag{48}$$

This result mirrors that for the onset of flow in a uniform sheet down an incline, which has been suggested as a practical rheometer[31]. Similarly, one could envision using a slowly rotating drum to infer yield stresses.

The second term in (42) illustrates how corrections to q arise at $O(\Lambda^{-n})$. As can be seen from combining (42) and (44), this suggests that η_{max} and $\theta_{max} \sim \sin^{-1}(\mathrm{Bi}/\eta_{max})$ also contain corrections terms of that order. Thus, η_{max} and θ_{max} should converge to the plastic limit at the rate Λ^{-n}, as appears to be borne out in figure 8(c,d), in which these quantities are plotted against Λ^{-n}. However, as evident from the second term on the right of (46), there are also potentially larger corrections of $O(\Lambda^{-\frac{n}{n+1}})$. In fact, these corrections, which do ultimately control the convergence to the plastic limit, are hidden at relatively small values

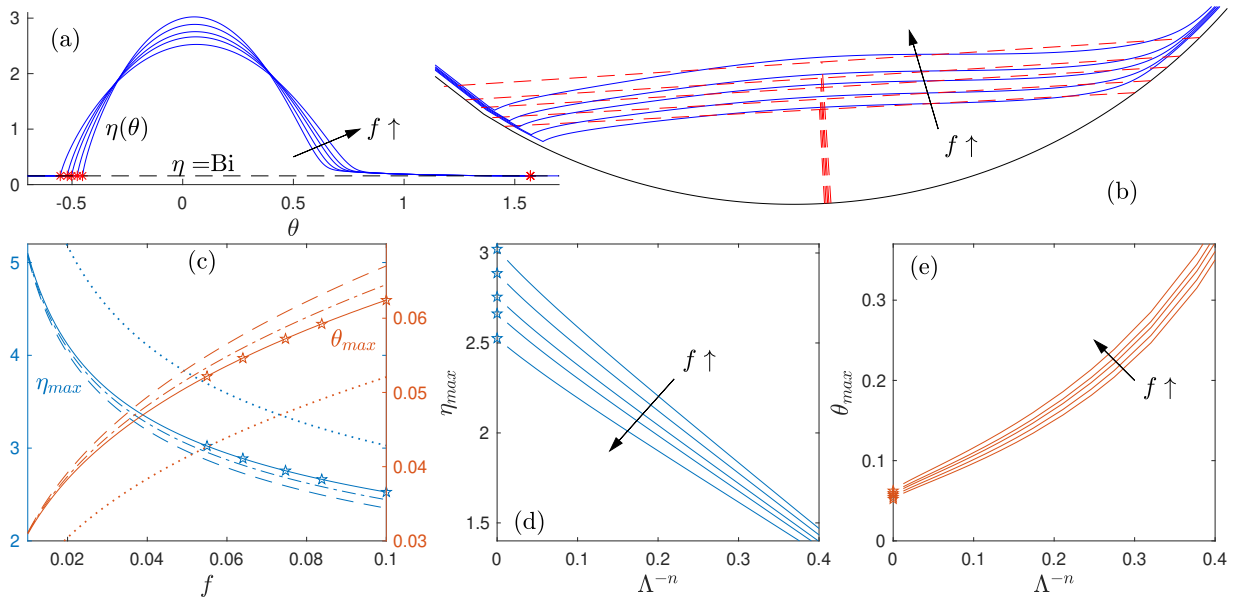

FIG. 8. (a) Solutions in the plastic limit for $f = 0.055$, 0.064, 0.0747, 0.0838 and 0.1, with $S = 0$ and $(n, \mathrm{Bi}) = (0.38, 0.158)$; the stars indicate the yield points. The solutions are replotted as they would appear in the drum in (b), with the dashed lines indicating the approximation of the pool as a segment given by (A2) and (48). (c) Peak depth η_{max} and its position θ_{max} plotted against f. The dotted lines show (43) and (48); the improvements in (44) and (A2) are shown by dashed and dot-dashed lines, respectively. The stars indicate the values of f shown in (a). (d,e) Peak depth η_{max} and its position θ_{max} plotted against Λ^{-n} for the same values of f as in (a). The limits for $\Lambda \to \infty$, from (b), are indicated by stars.

of Λ^{-n} in figure 8(c,d). Instead, a conspiracy between the parameter settings ensures that the intermediate rate of convergence Λ^{-n}, or Ω^n in terms of the dimensional rotation rate, is more obvious.

IV. DRAINAGE SOLUTIONS

If the flux function $Q(\eta, \Gamma)$ in (32) is modified to delete the first term, the background rotation of the cylinder is removed (the scalings of the problem then employ an arbitrary rate Ω, which could be removed by another scaling of time; we avoid this extra rescaling here). The evolution equation then models the gravitationally driven drainage of the fluid coating. For a viscous fluid, the outcome of such drainage is a flat pool at the bottom of the cylinder with an ever-thinning residual film elsewhere. When there is a yield stress, however, drainage ends with pools with finite free surface slopes, analogous to the slumped states resulting from dambreaks on flat surfaces[22,32–35], together with a residual film of finite thickness.

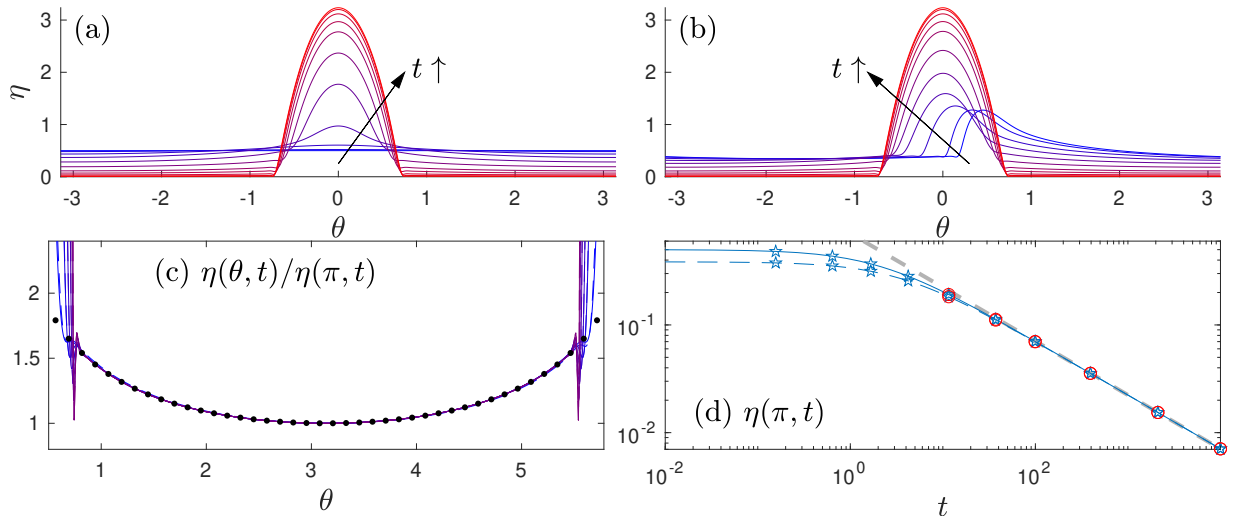

FIG. 9. Two viscous drainage solutions for $f = 0.0838$ and $S = 10^{-4}$ ($\Lambda = 1$). The initial conditions are (a) $\eta(\theta, 0) = \frac{1}{2}$ and (b) a steady rotating solution with $\Lambda = 1$. The residual film is scaled by $\eta(\pi, t)$ in (c), and the time series of $\eta(\pi, t)$ is plotted in (d). The times of the snapshots in (a) and (b), which increase from blue to red, are plotted as dots in (d); the circles show the slightly fewer snapshots plotted in (c). The dots in (c) and grey dashed line in (d) show the prediction from (50) with $n = 1$.

A. Viscous (and power-law) drainage

Solutions for viscous drainage ($(n, \mathrm{Bi}) = (1, 0)$) are shown in figure 9. These initial-value problems commence with either a uniform film ($\eta(\theta, 0) = \frac{1}{2}$) or a state corresponding to a steadily rotating solution (with $\Lambda = 1$), simulating the sudden stop of the cylinder. The latter is left-right asymmetrical at the outset, but the solution quickly symmetrizes and the long-time behaviour of both solutions is similar. In particular, a slowly growing pool forms the bottom of the cylinder, as a residual film slowly drains downwards.

The long-time drainage solutions can be described analytically, as follows. First, over the pool, $\Gamma \sim \sin\theta + f\eta_\theta \cos\theta \sim 0$, with the approximate solution in (38). Second, over the film in the right-half of the cylinder ($0 < \theta < \pi$ and $\sin\theta > 0$), we have $\Gamma \sim \sin\theta$ and the evolution equation for $\mathrm{Bi} = 0$ reduces to

$$\eta_t - \Lambda[\eta^{2+\frac{1}{n}}(\sin\theta)^{\frac{1}{n}}]_\theta \sim 0 \tag{49}$$

(the long-time solution is symmetric, with $\eta(\theta, t) = \eta(-\theta, t)$). We note the separable solution,

$$\eta \sim \left[\frac{n}{(2n+1)\Lambda t}(\sin\theta)^{-\frac{n+1}{2n+1}} \int_\theta^\pi (\sin\theta)^{-\frac{1}{2n+1}} \mathrm{d}\theta\right]^{\frac{n}{n+1}} \tag{50}$$

which is compared to late-time numerical solutions in figure 9(c) for $n = 1$. The viscous film therefore drains as $t^{-\frac{1}{2}}$, as seen in figure 9(d). For $n < 1$, and the fluid becomes more shear thinning, the film drains more slowly as $t^{-n/(n+1)}$.

B. Drainage with a yield stress

Sample drainage solutions with a yield stress are displayed in figure 10. In the first of these, a flat pool at the bottom of the cylinder is suddenly rotated clockwise by 90°, and then allowed to slump to rest. The slump leaves behind a thin residual layer held at the yield stress (with $\eta \approx \mathrm{Bi}/|\sin\theta|$), spanning the location of the original pool. To generate a second solution, the final state from this slump is then rotated again by 90°, and left to slump again. Repeating this exercise two more times then gives four rotate-and-slump solutions, the final states of which are shown in figure 10(b). As the slumps are sequentially rotated, more fluid is left coating the cylinder and the area of the pool slowly decreases. For the final rotate-and-slump, the slumping fluid encounters the residual film left by the first slump on its way to the bottom of the cylinder.

The rotate-and-slump scenario leads to fluid slumping in one direction and an asymmetrical final deposit. Other examples, with less asymmetry are shown in figure 10(c,d). In these two cases, the initial conditions correspond to steady solutions for a rotating drum at two different rotation rates, each simulating a sudden stop. Because these solutions feature both an offset pool and a residual film thickened by rotation, when the fluid begins to drain, flow occurs down both sides of the cylinder. For the slower example in (c), the drainage down the left side of the cylinder is mild and the final deposit is almost as asymmetric as those from the rotate-and-slump examples. More drainage arises on the left for the faster example in (d).

When all the drainage takes place down one side, the final state is the same as the plastic limit ($\Lambda \to \infty$) of the steadily rotating solutions of §III C, except for any differences arising over the plugged sections of the residual film. This correspondence arises because, for final solution from the initial-value problem to approach rest, the yield condition $\mathcal{Y} \to 0$ must be reached over the flowing regions, implying (47). The limiting, steadily rotating solution for $\Lambda \to \infty$ is also plotted in figure 10(c). Despite the common form expected for the solutions over the yielded sections of the film, differences can remain over the plugs, since the rotating solution has $\eta = \mathrm{Bi}$ here, whereas the drainage solution may have $\eta < \mathrm{Bi}$.

Finally, the last example of figure 10(e) shows a slump from a uniform initial coating ($\eta(\theta, 0) = \frac{1}{2}$). This example is necessarily left-right symmetrical. The maximum depth also now no longer arises at the centre of the pool, where, instead, a mild minimum arises at the meeting of the counter-flowing drainage currents. The final state in this case is more directly computed by neglecting surface tension and integrating the ODE (47) from a trial value of η at $\theta = 0$, to the right and up to to $\theta = \frac{1}{2}\pi$. As the integration of (47) proceeds past the pool, the solution converges to the residual film, with $\eta \approx \mathrm{Bi}/\sin\theta$, which can then be used to continue the solution past the singular point $\theta = \frac{1}{2}\pi$ (as in the construction of the Appendix) and up to the plug at $\theta \approx \sin^{-1}(2\mathrm{Bi})$, where $\eta = \frac{1}{2}$. The solution for $\theta < 0$ is then given by reflection. This computation can be iterated again, adjusting the value of η at $\theta = 0$, such that the constraint (33) is eventually satisfied. The dots in figure 10(e) show the result of this construction. There is a minor difference between the construction and the final snapshot of the initial-value computation because surface tension plays a slight role near the centre of the pool for the latter (*cf.* figure 5), smoothing out the corner at the local minimum.

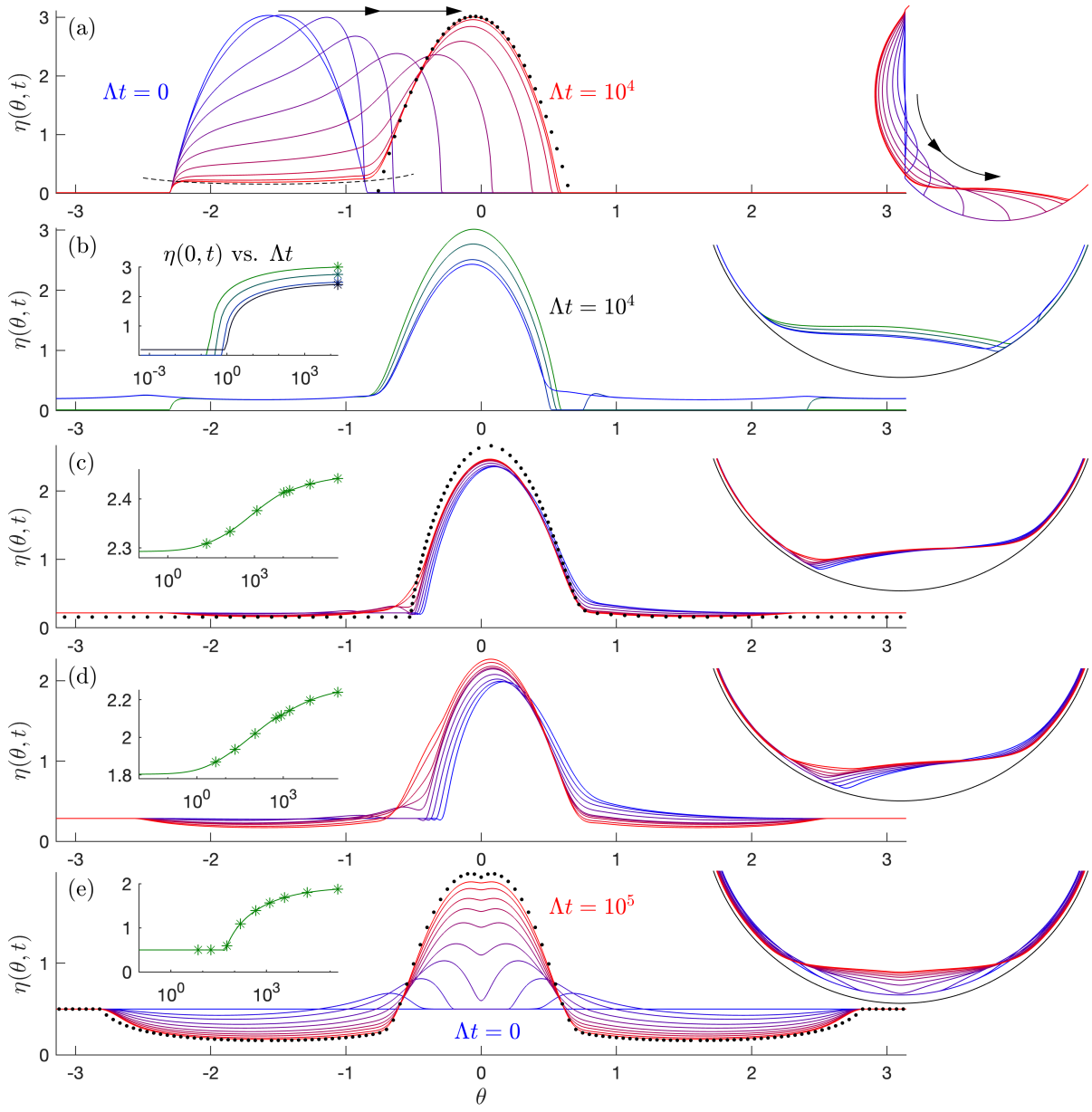

FIG. 10. Drainage solutions for $(f, \mathrm{Bi}, n, S) = (0.0838, 0.158, 0.38, 10^{-4})$. In (a), a flat pool at the bottom of the cylinder is suddenly rotated clockwise by 90 degrees; shown are snapshots of $\eta(\theta, t)$ as the fluid slumps back to rest (from blue to red). The black dashed line shows $\eta \sim \mathrm{Bi}/|\sin\theta|$, and the dots plot (38). In (b), the final state is plotted, along with three others generated by successive rotate-and-slump events (see main text, with the progression plotted from green to blue). In (c) and (d), slumps from steady states in rotating drums are used (respectively, $\Lambda = 684$ and 68.4), simulating sudden stops. For (e), the slump occurs from a uniform coating ($\eta(\theta, 0) = \frac{1}{2}$). The right-hand insets show the solutions as they would appear in the cylinder, and the insets on the left show the time series of $\eta(0, t)$, with the stars showing the times of the snapshots in the main panels. For the solutions in (a) and (b), to avoid any issues with contact lines, a thin pre-wetted film of thickness 10^{-2} is included to ensure that $\eta(\theta, 0) > 0$ everywhere. The black dots in (c) and (e) plot the results predicted in the plastic limit for $S = 0$ (*i.e.* from integrating (47)) subject to either $\eta = \mathrm{Bi}$ at the left of the pool and $\theta = \frac{1}{2}\pi$ (panel (c)), or symmetry about $\theta = 0$ (panel (e)).

V. EXPERIMENTS

To complement the theoretical analysis, we conducted some experiments using an aqueous suspension of Carbopol in an acrylic cylinder; see figure 11. The Carbopol (Ultrez 21) suspension was neutralized with sodium hydroxide and had a concentration of about 0.2% and density $\rho \approx 1\mathrm{g/cm}^3$. A Herschel-Bulkley fit of the flow curves measured in a rheometer (Kinexus, Malvern, fitted with roughened parallel plates) gave the parameters,

$$\tau_{\mathrm{Y}} = 18 \text{ Pa}, \quad K = 13 \text{ Pa s}^n, \quad n = 0.38. \tag{51}$$

The inside surface of the cylinder was roughened with 60 grit sandpaper in an effort to eliminate the effective slip that Carbopol suffers against acrylic surfaces[25,36,37]. The front and back surfaces were left smooth, however, in order to allow the Carbopol to slide more freely over them, and try to maintain a more two-dimensional flow pattern. The cylinder, with inside diameter of 27.8cm and a length of 13.1cm, was placed on friction rollers attached to a stepper motor to drive a prescribed rotation.

To conduct a set of experiments, fluid was first loaded into the drum up to a given fill fraction. The drum then sealed, to minimize evaporation, and its rotation rate was first increased and then decreased in a step-like manner to sweep over a range of Ω. At each rotation rate, the free surface was imaged through the clear, front, acrylic face. Figure 11 shows two examples illustrating our fit of the surface profile using image processing (based on a threshold intensity for the difference between the blue and red channels of the RGB image). Whenever the fluid drained into a pool near the bottom of the cylinder, a steady state was reached. Several images were taken of such steady states and the extracted profiles combined to furnish an average. Except at the lowest rotation rates, these averages were taken over at least two rotations of the drum. For the lowest rotation rates, each average spanned more than thirty minutes, and the sweep in rotation rate performed over the course of hours.

As a comparison against a suite of control experiments with a Newtonian fluid, we also conducted tests in which the cylinder was filled with golden syrup (density $\rho = 1.54\ \mathrm{g/cm}^3$, viscosity 11 Pa s) to a fill fraction of $f = 0.0737$. Results for these controls are shown in figure 12. Displayed are a selection of measured depth profiles, and the peak depth and its position, plotted against rotation rate. The figure includes corresponding results from the theoretical model (for $n = 1$ and $\mathrm{Bi} = 0$, adopting either $S = 0$ or $S = 10^{-5}$, the latter corresponding to a dimensional surface tension parameter of $0.5\mathrm{Nm}^{-1}$; the overlap of the two theoretical lines highlights how the results are insensitive to surface tension effects). There is some agreement between theory and experiment, although the location of the pool is somewhat shifted between the two, particularly at higher rotation rate. Better agreement is reported by Tirumkudulu & Acrivos[7] who used a different drum geometry and fluid, but similar fill fractions. In particular their drum was rather longer than ours (in comparison to drum radius). It is therefore possible that the three-dimensionality of the flow field is responsible for the discrepancy in our experiments. In fact, there were noticeable residual films of syrup coating annuli on the front and back faces of the cylinder, the length of the pool was comparable to the drum width, and the shape of the pool became visibly more three dimensional in the experiments as the rotation rate increased (*cf.* figure 11). Nevertheless, repeating the experiments in a longer drum did not substantially change the results for the peak depth and its position; see figure 12.

Figure 13(a) shows a sequence of surface profiles for increasing rotation rate for experiments with Carbopol at fill fraction $f = 0.0838$. These tests correspond to a set of values

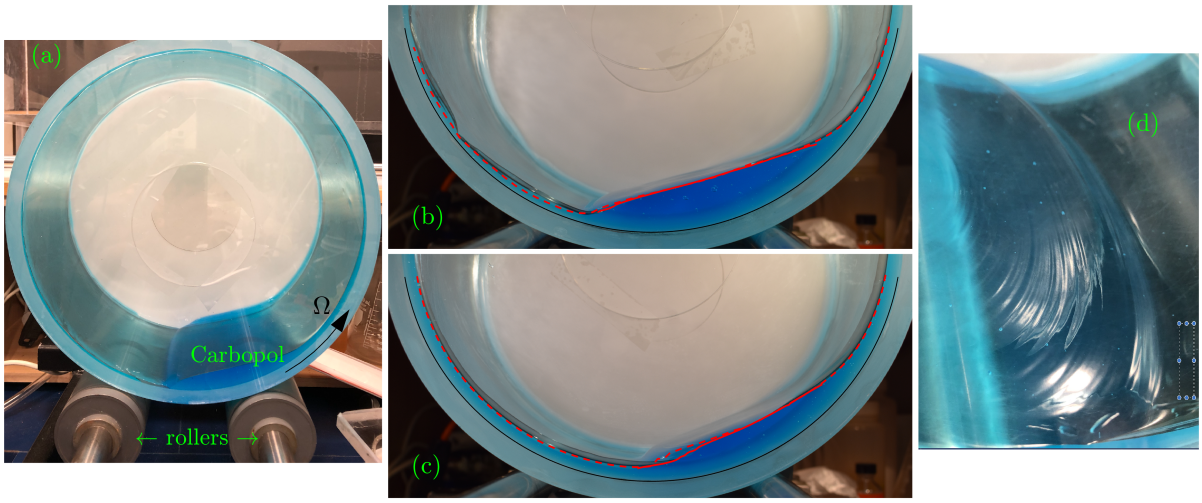

FIG. 11. Images of the rotating drum, with fits to the surface profile of an enclosed Carbopol suspension, dyed blue with food colouring. In (b) and (c), with rotation rates are $\Omega = 0.024$ rad/s and 0.14 rad/s, respectively, two fits are shown. The solid line shows a fit to the profile along the front face; the dashed line is a fit with a weaker threshold that captures more of the profile further inside the drum as well as the residual film outside the pool. The two fits are mostly the same in (b), but at the faster rotation speed in (c), the three-dimensionality of the front edge of the pool becomes more pronounced; the second fit takes some account of this to furnish a more averaged profile. An oblique view of a three-dimensional surface profile is shown in (d), along with some surface wrinkles generated by the flow dynamics. $f = 0.0838$.

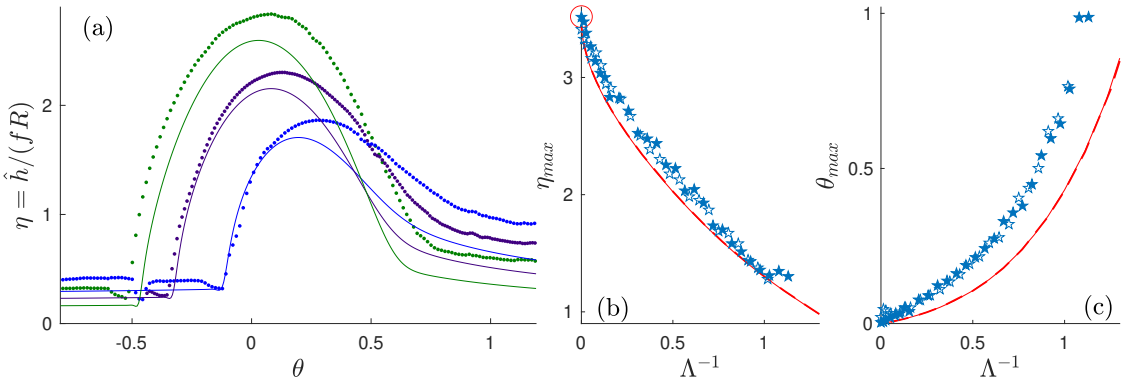

FIG. 12. (a) Experimental syrup profiles at the dimensionless rotation rates, $\Lambda^{-1} = 3\mu\Omega/(\rho g R f^2) = (0.21, 0.43, 0.67)$ (from green to blue), with $f = 0.0687$. (b) Maximum depths $\hat{h}_{max}$ and (c) angular positions θ_{max} plotted against Λ^{-1}. The open stars correspond to the drum with inner radius and width, $(R, W) = (27.8, 13.1)$cm; the filled stars correspond to a wider drum with $(R, W) = (28.8, 20)$cm. The solid and dashed lines in (b) and (c) show equivalent theoretical results with $S = 10^{-5}$ and $S = 0$, respectively. The red circle in (b) shows the depth expected for $\Omega = 0$. The fits of the surface in the experiments are all to the syrup profile as observed at the front face of the drum.

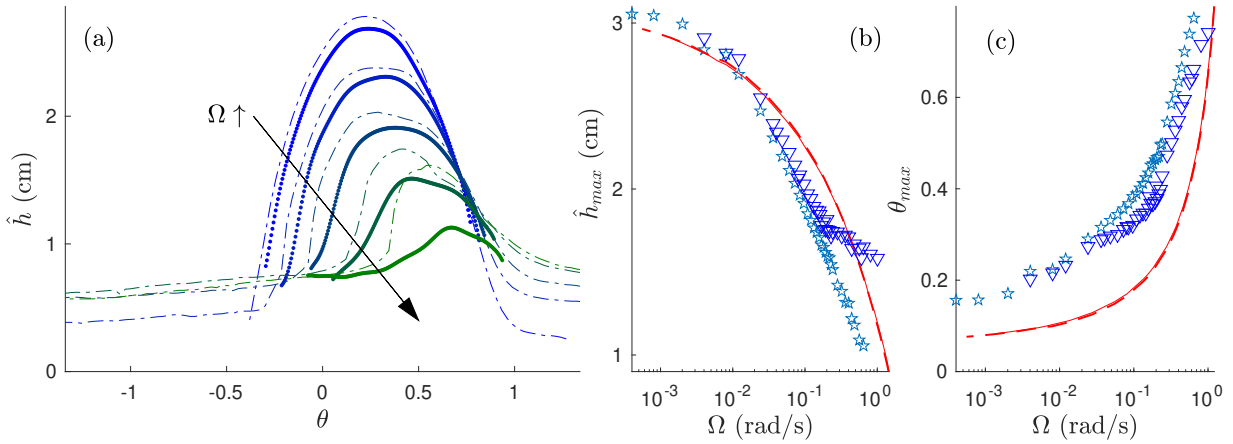

FIG. 13. (a) Experimental Carbopol profiles for $f = 0.0838$ at the rotation rates, $\Omega = (0.012, 0.036, 0.097, 0.24, 0.44)$ rad/s, corresponding to $\Lambda = (457, 152, 57, 23, 12)$ (from blue to green) and $(n, \mathrm{Bi}) = (0.38, 0.158)$. The dots show the profiles fitted for the front face; the dash-dotted lines show the fits including more of the interior (see figure 11). (b) Maximum depths $\hat{h}_{max}$ and (c) angular positions θ_{max} plotted against rotation rate Ω. The solid and dashed lines in (b) and (c) translate the theoretical results (with $S = 10^{-4}$ and $S = 0$, respectively) from figure 4; the stars and triangles show the two fits (front face and including interior, respectively).

for the dimensionless parameter Λ similar to those in figure 4. Also plotted are the (dimensional) maximum depth, $\hat{h}_{max}$, and its angular location, θ_{max}, against Ω for a much wider set of experiments. Again, there is some qualitative agreement between the experimental results in figure 13 and those predicted theoretically, but the two disagree quantitatively. As in the Newtonian case, this disappointment may arise partly because of the three-dimensionality of the experimental flows. The effect of the third dimension is illustrated by the comparison between the profiles extracted at the front face of the drum, and those found when the thresholding in the image analysis is weakened to capture more of the profile further inside the drum as well as the residual film outside the pool (figure 11). At lower rotation rates, the two profiles largely match, but they disagree significantly for $\Omega > 0.1$ rad/s.

The discrepancy between theory and experiment may also arise because the fill fraction in the experiments, $f = 0.0838$, corresponds to $\epsilon \approx 0.3$ in the asymptotic theory. The relatively large size of ϵ suggests that the theory may not be very accurate. Indeed, the surface slopes observed experimentally were fairly steep, potentially invalidating the shallow-flow theory. Imaging problems (the need to view the flow through the sidewall and the local meniscus there) and the incomplete elimination of wall slip may also both contribute.

Experimental results closer to the plastic limit ($\Omega \to 0$) and for varying fill fraction are shown in figure 14. Here, following the theoretical predictions in figure 8, we plot the maximum depth and its angular position, $h_{max} = \hat{h}_{max}/R \equiv f\eta_{max}$ and θ_{max} against Ω^n. According to the theory, this power of rotation rate should straighten the data into straight lines. Figure 14 does indeed suggest this to be the case: the data is certainly straightened in comparison to a plot using Ω, although any exponent between 0.3 and 0.45 is as successful. Linear fits to the data plotted in this way can be used to estimate the limiting maximum depth and its position for $\Omega \to 0$, as also shown in the figure. The limit for the maximum depth compares somewhat favourably with the prediction in (44) (with $q = \mathrm{Bi}$), but the experimental results for the position are again too high in comparison to (48).

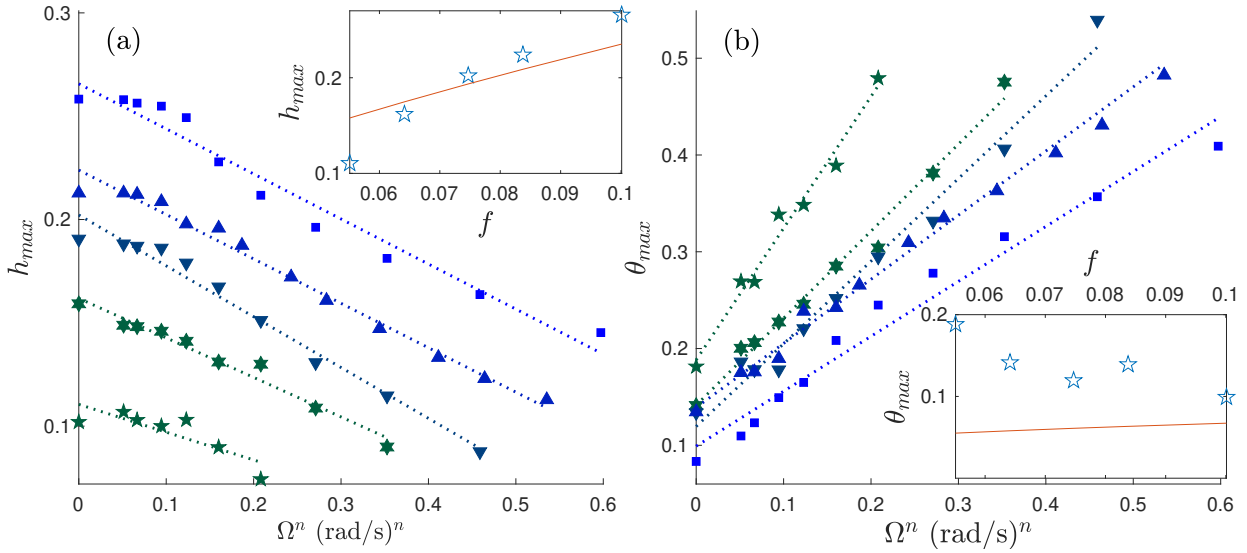

FIG. 14. Experimental results for Carbopol with varying fill fraction ($f = 0.055$, 0.064, 0.0747, 0.0838 and 0.1, from green to blue), showing (a) maximum depth $h_{max} = \hat{h}_{max}/R \equiv f\eta_{max}$ and (b) position θ_{max} plotted against Ω^n (with Ω in rad/s). The dotted lines show linear fits, and the insets plot the implied intercepts (for $\Omega \to 0$) against f. The solid lines in the insets show (44) and (48) (with $q = \mathrm{Bi}$).

Finally, figure 15 displays some experimental results for the drainage problem. As predicted theoretically, the final state reached after drainage supports finite surface slopes and has a varying degree of left-right symmetry depending on how the draining flow was initiated, and, in particular, how much of the fluid drained down each side. The experiments shown in figure 15 roughly correspond to the theoretical solutions plotted in figure 10. In particular, shown are a succession of rotate-and-slump events, or adjustments taking place when a rotating cylinder, with its fluid coating in steady state, is abruptly stopped. For the final example of the latter three tests, the cylinder was rotated at sufficiently high speed that the fluid coating became relatively uniform; the drainage that resulted after stopping the cylinder was then almost left-right symmetric.

VI. CONCLUSIONS

In this paper, we have considered the viscoplastic version of the problem of viscous rimming flow around a rotating drum. Our analysis extends some earlier work that considered relatively rapidly rotating coatings of either power-law or Bingham fluids[3,15]. In particular, we allowed the fluid to be described by the Herschel-Bulkley constitutive law and to rotate more slowly, so that the fluid mostly gathers into a pool near the bottom of the drum. The main effect of introducing a yield stress is to arrest and thicken the residual film coating the cylinder outside the pool, thereby drawing more fluid out of the pool and forcing that feature to ascend up the side of the drum. We complemented the theory with some experiments with a Carbopol suspension, finding qualitative, but not quantitative agreement. The discrepancies between theory and experiment may result from, in the experiments, three-dimensional flow fields (the theory is two-dimensional), the presence of wall slip[25,36,37], or

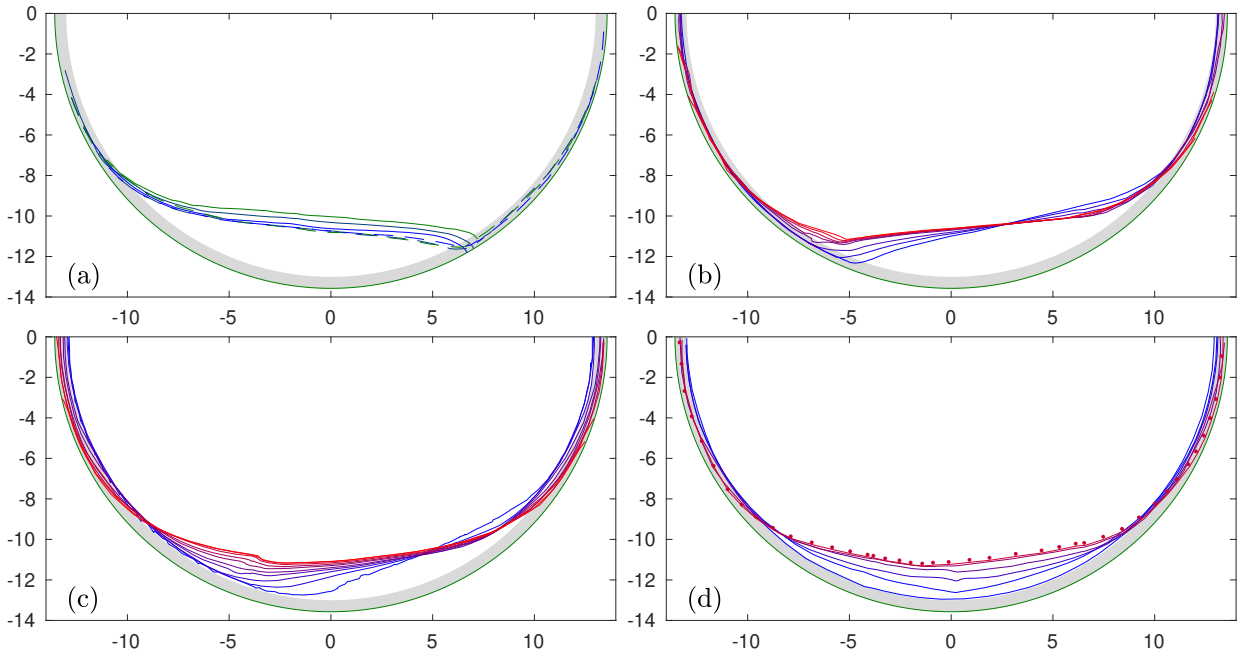

FIG. 15. Experimental drainage tests with Carbopol; $f = 0.0838$ and $(n, \mathrm{Bi}) = (0.38, 0.158)$. In (a), a mound of material emplaced at the bottom of the cylinder was rotated clockwise by about 90° to force an adjustment to rest (green curve). The new mound was then rotated again twice (by a similar angle) to prompt two more adjustments (each leaving a longer residual coating behind; solid lines, from green to blue). The cylinder was then rotated three more times, with the fluid now encountering the coating from the previous rotate-and-slump events (dashed lines, from green to blue). In panels (b,c,d), steady-state cylinders rotating with rates of $\Omega = 0.008$ rad/s, 0.08 rad/s and 2 rad/s were abruptly stopped, leaving the fluid to drain (outlines from blue to red). In (d), the dots show the outcome of a repetition of the experiment. In all panels, the shaded region indicates the uniform film expected with a fill fraction of $f = 0.0838$, and the units are in cm.

overly steep surface slopes (we employ a shallow flow theory).

A distinctive feature of shallow viscoplastic fluids is the development of a superficial, plug-like flow. In most situations, this plug-like region cannot be rigid because there must also be weak straining motion along the film, leading to previous work referring to this region as a pseudo-plug[20,23,24]. Such pseudo-plugs also feature in the viscoplastic rimming flows considered here. Nevertheless, in some settings, the pseudo-plug can itself fall below the yield stress, to lead to genuine floating plugs[19,38,39]. In the curved geometry of the shallow coating flow, it is more difficult to understand how the pseudo-plug could become truly rigid in the present context, except near the angular positions where the speed of the pseudo-plug becomes relatively flat near an extremum. Such positions do arise near the centre of the pool, suggesting that this feature could partly plug up. In fact, it is possible to extend the analysis presented in Refs. 19, 23, 38, and 39 to explicitly build in the plugged parts of the pool. It is also conceivable that when the film is no longer shallow (at higher fill fractions and slow rotation rates), the entire pool plugs up. Indeed, in some experiments that we conducted with a thicker Carbopol suspension (not reported in the main text), pools with complicated surface features could be emplaced in the drum; these features survived the rotation of the drum, persisting for the length of the experiment.

Rotating drums are popular devices to study the flow of various materials, besides viscous fluids[11]. In particular, rotating drums have been used to help formulate constitutive theories for granular media[40]. At low rotation rates, granular flow in rotating drums becomes unsteady, continuous avalanching (or "rolling") becoming replaced by episodic avalanching ("slumping"; *e.g.* Refs. 11 and 41). Although this transition may be a unique feature of a granular medium, one of our interests in conducting the experiments of the present work was to explore whether non-ideal viscoplastic effects near the yield stress[20] might prompt analogous or novel, unsteady flow dynamics at very low rotation rates. None were evident for the Carbopol suspension, suggesting that a fluid with more hysteretic material behaviour might be needed in the drum[42–44]. At higher rotation rates, however, surface features with a relatively small spatial scale did become evident for the Carbopol (figure 11(d)). These features resembled the wrinkling of elastic or viscous films[45–47] and may have some correspondence with surface patterns seen in other viscoplastic flows[48].

Finally, for Newtonian rimming flow, it has been of interest to move beyond the Stokes limit and add inertia to the thin film problem in order to explore the potential for hydrodynamic instability (*e.g.* Ref. 49). One could also continue along this vein for viscoplastic rimming flow. Indeed, one expects that inertial visoplastic surges should become unstable and time-dependent at sufficiently high speeds, a possibility that does not appear to have been recorded in the conveyor belt experiments of Chambon and co-workers, but was noted in related numerical computations[19]. Time-dependent motions were observed in our rotating drum at high rotation rates, but at these speeds the flow was also fully three-dimensional and well beyond the scope of our two-dimensional theory (fluid flowed sideways, collecting into localized patches that could be carried all the way around the drum or dripped off the upper surface).

ACKNOWLEDGMENTS

TVB is supported by the Leverhulme Trust Early Career Fellowship ECF-2022-584.

Appendix A: Steady solutions without surface tension

Without surface tension, the steady solutions, with $q = Q(\eta, \Gamma) = constant$, satisfy a first-order differential-algebraic problem. For the Newtonian problem, Tirumkudulu & Acrivos[7] pointed out some of the numerical difficulties inherent in the Newtonian version of this problem. For small f, however, the solutions can be found using a relatively simple shooting technique: we first parametrize the solution by $\eta_{max} = \eta(\theta_{max})$, the height of the peak in the pool. Because the flux is given by (40) for $n = 1$, or more generally by (41), the peak location θ_{max} (where $\eta_\theta = 0$) follows from $q = Q(\eta_{max}, \sin\theta_{max})$. We may then integrate the ODE for $\eta(\theta)$ to the left and right of the peak. Progressing to the right, the pool ends when the solution reaches the residual film, dictated approximately by $q = Q(\eta, \sin\theta)$, or (39) for $n = 1$. The integration can then be terminated before reaching the singular point at $\theta = \frac{1}{2}\pi$, and the solution continued using the approximation for the film. Further right, the film encounters a yield point where $\eta = q$, and the film plugs up thereafter. To the left, the integration either again reaches the film solution, or hits another yield point (again with $\eta = q$). Over the rigid sections, the film thickness maintains the value $\eta = q$, until one reaches the other yielded section surrounding $\theta = \pi$, where the solution is again given

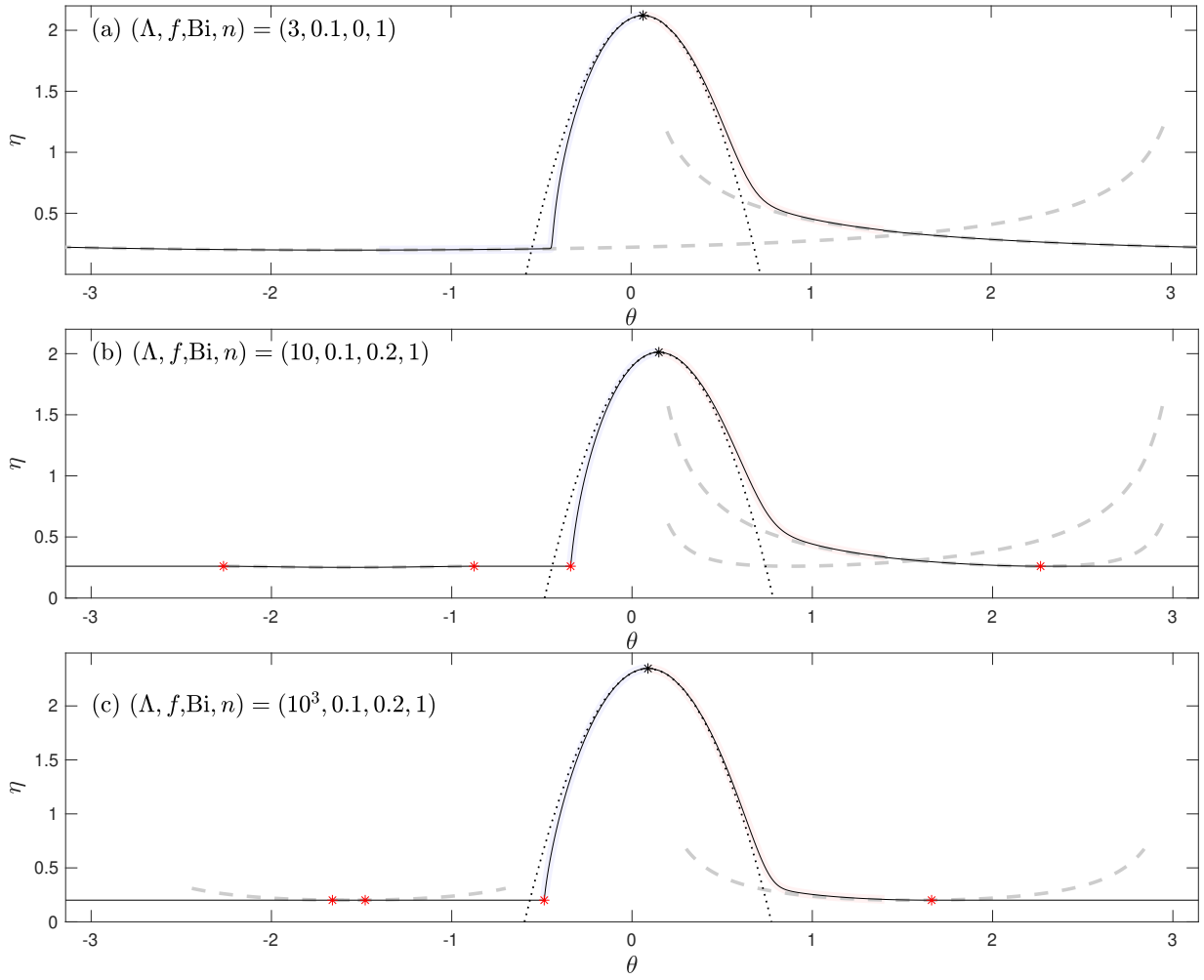

FIG. 16. Construction of steady solutions without surface tension for (a) Newtonian and (b,c) Bingham fluid (parameter settings indicated). Beginning from the peak, we integrate left (blue solid) and right (red solid) until the solution converges to one of the residual film solutions (grey dashed) or a yield point (red stars). Over any plugs, $\eta = q$. The thin black line shows the constructed solutions. The dotted line shows the approximation for the pool in (38). For (c), the steady solution is given approximately by (47) and the film solution is just $\eta \approx \mathrm{Bi}/|\sin\theta|$ or $\eta \approx \mathrm{Bi}$.

approximately by $q = Q(\eta, \sin\theta)$. In the Newtonian case ($\mathrm{Bi} = 0$ and $n = 1$), the strategy is the same, but for the omission of any plugs. The last part of the exercise is to iterate the procedure, adjusting the value of η_{max} until the mass constraint (33) is satisfied. Sample constructions are shown in figure 16.

Evidently, when the pool ends to the left at a yield point, the free surface slope becomes discontinuous (see figure 5). This feature becomes smoothed by surface tension to generate the viscoplastic wavetrain seen in figures 6 and 7, and discussed more thoroughly by Jalaal *et al.*[29,30]. The transition from the pool to the film is smoother to the right, and only features undulations with sufficient surface tension (*cf.* figure 5).

For $\Lambda \gg 1$, we enter the plastic limit of the problem in which the bulk of the fluid flow is controlled by the yield stress. In this situation, the pseudo-plug fills most of the layer, $\mathcal{Y} \to 0$, and $q \to \mathrm{Bi}$ (see §III B). The solution can then be written down more explicitly:

the residual film is mostly plugged up, with $\eta = q = \mathrm{Bi}$, except over the region spanning the edge of the pool to $\theta = \pi$. Here, and over the pool, the problem reduces to the ODE (47), with the approximate solution discussed in §III C. The contributions of each region to the constraint (33) is as follows: the area of the pool is approximately $\frac{4}{3}\eta_{max}\sqrt{2f\eta_{max}}$ (see §6), whereas the rigid section of the residual film has area $\frac{3}{2}\pi\mathrm{Bi}$. The yield section of the film extends from the right-hand border of the pool, at position $\theta_{max} + \sqrt{2f\eta_{max}} \sim O(f^{\frac{1}{3}})$ to $\frac{1}{2}\pi$; the corresponding area is then, to leading-order, $\frac{1}{3}\mathrm{Bi}\log f^{-1}$. The constraint then implies that

$$\frac{4}{3}\eta_{max}\sqrt{2f\eta_{max}} + \frac{3}{2}\pi\mathrm{Bi} + \frac{1}{3}\mathrm{Bi}\log f^{-1} = \pi, \tag{A1}$$

or

$$\eta_{max} = (\pi - \tfrac{3}{2}\pi\mathrm{Bi} - \tfrac{1}{3}\mathrm{Bi}\log f^{-1})^{\frac{2}{3}}\left(\frac{9}{32f}\right)^{\frac{1}{3}}. \tag{A2}$$

This approximation fails for $f \to 0$, corresponding to a fill-fraction regime where the left-hand edge of the yielded residual film has greatest area.

[1] H. K. Moffatt. Behaviour of a viscous film on the outer surface of a rotating cylinder. J. de Méc., 16(5):651–673, 1977.

[2] S. B. G. OBrien and E. G. Gath. The location of a shock in rimming flow. Phys. Fluids, 10(4):1040–1042, 1998.

[3] R. E. Johnson. Steady-state coating flows inside a rotating horizontal cylinder. J. Fluid Mech., 190:321–342, 1988.

[4] J. Ashmore, A. E. Hosoi, and H. A. Stone. The effect of surface tension on rimming flows in a partially filled rotating cylinder. J. Fluid Mech., 479:65–98, 2003.

[5] E. S. Benilov, M. S. Benilov, and Natalia Kopteva. Steady rimming flows with surface tension. J. Fluid Mech., 597:91–118, 2008.

[6] André v B Lopes, Uwe Thiele, and Andrew L Hazel. On the multiple solutions of coating and rimming flows on rotating cylinders. J. Fluid Mech., 835:540–574, 2018.

[7] Mahesh Tirumkudulu and Andreas Acrivos. Coating flows within a rotating horizontal cylinder: Lubrication analysis, numerical computations, and experimental measurements. Phys. Fluids, 13(1):14–19, 2001.

[8] S T Thoroddsen and L Mahadevan. Experimental study of coating flows in a partially-filled horizontally rotating cylinder. Exp. Fluids, 23(1):1–13, 1997.

[9] A E Hosoi and L Mahadevan. Axial instability of a free-surface front in a partially filled horizontal rotating cylinder. Phys. Fluids, 11(1):97–106, 1999.

[10] E. S. Benilov and S. B. G. OBrien. Inertial instability of a liquid film inside a rotating horizontal cylinder. Phys. Fluids, 17(5):052106, 2005.

[11] Gabriel Seiden and Peter J Thomas. Complexity, segregation, and pattern formation in rotating-drum flows. Rev. Mod. Phys., 83(4):1323, 2011.

[12] Francis Patton Bretherton. The motion of long bubbles in tubes. J. Fluid Mech., 10(2):166–188, 1961.

[13] Simon DR Wilson. The drag-out problem in film coating theory. J. Eng. Math., 16(3):209–221, 1982.

[14] Steven J Weinstein and Kenneth J Ruschak. Coating flows. Annu. Rev. Fluid Mech., 36:29–53, 2004.

[15] A B Ross, S K Wilson, and B R Duffy. Thin-film flow of a viscoplastic material round a large horizontal stationary or rotating cylinder. J. Fluid Mech., 430:309–333, 2001.

[16] G. Chambon, A. Ghemmour, and D. Laigle. Gravity-driven surges of a viscoplastic fluid: An experimental study. J. Non-Newtonian Fluid Mech., 158:54–62, 2009.

[17] G. Chambon, A. Ghemmour, and M. Naaim. Experimental investigation of viscoplastic free-surface flows in a steady uniform regime. J. Fluid Mech., 754:332–364, 2014.

[18] P. Freydier, G. Chambon, and M. Naaim. Experimental characterization of velocity fields within the front of viscoplastic surges down an incline. J. Non-Newtonian Fluid Mech., 240:56–69, 2017.

[19] Y Liu, N J Balmforth, and S Hormozi. Viscoplastic surges down an incline. J. Non-Newtonian Fluid Mech., 268:1–11, 2019.

[20] N. J. Balmforth, I. Frigaard, and G. Ovarlez. Yielding to stress: Recent developments in viscoplastic fluid mechanics. Ann. Rev. Fluid Mechanics, 46:121–146, 2014.

[21] K. F. Liu and C. C. Mei. Slow spreading of a sheet of Bingham fluid on an inclined plane. J. Fluid Mech., 207:505–529, 1989.

[22] N. J. Balmforth, R. V. Craster, A. C. Rust, and R. Sassi. Viscoplastic flow over an inclined surface. J. Non-Newtonian Fluid Mech., 139:103–127, 2006.

[23] I. C. Walton and S. H. Bittleston. The axial flow of a Bingham plastic in a narrow eccentric annulus. J. Fluid Mech., 222:39–60, 1991.

[24] N. J. Balmforth and R. V. Craster. A consistent thin-layer theory for Bingham plastics. J. Non-Newtonian Fluid Mech., 84:65–81, 1999.

[25] Ariel P Dufresne, Thomasina V Ball, and Neil J Balmforth. Viscoplastic saffman–taylor fingers with and without wall slip. J. Non-Newtonian Fluid Mech., 312:104970, 2023.

[26] Lloyd N Trefethen. Spectral methods in MATLAB. SIAM, 2000.

[27] J Boujlel and P Coussot. Measuring the surface tension of yield stress fluids. Soft Matter, 9(25):5898–5908, 2013.

[28] B Géraud, L Jørgensen, L Petit, H Delanoë-Ayari, P Jop, and C Barentin. Capillary rise of yield-stress fluids. EPL (Europhysics Letters), 107(5):58002, 2014.

[29] M Jalaal and N J Balmforth. Long bubbles in tubes filled with viscoplastic fluid. J. Non-Newtonian Fluid Mech., 238:100–106, 2016.

[30] Maziyar Jalaal, Boris Stoeber, and Neil J Balmforth. Spreading of viscoplastic droplets. J. Fluid Mech., 914:A21, 2021.

[31] D De Kee, R P Chhabra, M B Powley, and S Roy. Flow of viscoplastic fluids on an inclined plane: evaluation of yield stress. Chem. Eng. Commun., 96(1):229–239, 1990.

[32] N. J. Balmforth, R. V. Craster, and R. Sassi. Shallow viscoplastic flow on an inclined plane. J. Fluid Mech., 470:1–29, 2002.

[33] G. P. Matson and A. J. Hogg. Two-dimensional dam break flows of Herschel-Bulkley fluids: The approach to the arrested state. J. Non-Newtonian Fluid Mech., 142:79–94, 2007.

[34] Y. Liu, N. J. Balmforth, S. Hormozi, and D. R. Hewitt. Two dimensional viscoplastic dambreaks. J. Non-Newtonian Fluid Mech., 238:65–79, 2016.

[35] Y. Liu, N J Balmforth, and S. Hormozi. Axisymmetric viscoplastic dambreaks and the slump test. J. Non-Newtonian Fluid Mech., 258:45–57, 2018.

[36] Howard A Barnes. A review of the slip (wall depletion) of polymer solutions, emulsions and particle suspensions in viscometers: its cause, character, and cure. J. Non-Newtonian Fluid Mech., 56(3):221–251, 1995.

[37] Masoud Daneshi, Jordan MacKenzie, Neil J Balmforth, D Mark Martinez, and Duncan R Hewitt. Obstructed viscoplastic flow in a hele-shaw cell. Phys. Rev. Fluids, 5(1):013301, 2020.
[38] I A Frigaard and D P Ryan. Flow of a visco-plastic fluid in a channel of slowly varying width. J. Non-Newtonian Fluid Mech., 123(1):67–83, 2004.
[39] N. J. Balmforth, R. V. Craster, and D. R. Hewitt. Building on oldroyds viscoplastic legacy: Perspectives and new developments. J. Non-Newtonian Fluid Mech., 294:104580, 2021.
[40] G D R MiDi. On dense granular flows. Eur. Phys. J. E, 14:341–365, 2004.
[41] N. J. Balmforth and J. N. McElwaine. From episodic avalanching to continuous flow in a granular drum. Granul. Matter, 20(3):52, 2018.
[42] Philippe Coussot, Quoc Dzuy Nguyen, H T Huynh, and Daniel Bonn. Avalanche behavior in yield stress fluids. Phys. Rev. Lett., 88(17):175501, 2002.
[43] Duncan R Hewitt and Neil J Balmforth. Thixotropic gravity currents. J. Fluid Mech., 727:56–82, 2013.
[44] Cassio M Oishi, Fernando P Martins, and Roney L Thompson. The avalanche effect of an elasto-viscoplastic thixotropic material on an inclined plane. J. Non-Newtonian Fluid Mech., 247:165–177, 2017.
[45] Dominic Vella, Mokhtar Adda-Bedia, and Enrique Cerda. Capillary wrinkling of elastic membranes. Soft Matter, 6(22):5778–5782, 2010.
[46] Sanjay Bhattacharya, R. V. Craster, and M. R. Flynn. Buckling of a thin, viscous film in an axisymmetric geometry. Phys. Fluids, 25(4):043102, 2013.
[47] Neil M Ribe, Mehdi Habibi, and Daniel Bonn. Liquid rope coiling. Ann. Rev. Fluid Mech., 44:249–266, 2012.
[48] Mathilde Maillard, Cédric Mézière, Pascal Moucheront, Christophe Courrier, and Philippe Coussot. Blade-coating of yield stress fluids. J. Non-Newtonian Fluid Mech., 237:16–25, 2016.
[49] ES Benilov and VN Lapin. Inertial instability of flows on the inside or outside of a rotating horizontal cylinder. J. Fluid Mech., 736:107–129, 2013.